Bioactive Materials 41 (2024) 537–552

Contents lists available at ScienceDirect

Bioactive Materials

journal homepage: www.keaipublishing.com/en/journals/bioactive-materials

A new silicon phthalocyanine dye induces pyroptosis in prostate cancer cells during photoimmunotherapy

Isis Wolf [a,b,c,1], Jonas Storz [d,1], Susanne Schultze-Seemann [a,b], Philipp R. Esser [b,e], Stefan F. Martin [b,e], Susan Lauw [f,g], Peer Fischer [h,i], Marie Peschers [a,b,c], Wolfgang Melchinger [b,j], Robert Zeiser [b,j], Oliver Gorka [b,k], Olaf Groß [b,k,l], Christian Gratzke [a,b], Reinhard Brückner [d,**], Philipp Wolf [a,b,*]

[a] Department of Urology, Medical Center – University of Freiburg, 79106, Freiburg, Germany
[b] Faculty of Medicine, University of Freiburg, 79106, Freiburg, Germany
[c] Faculty of Biology, University of Freiburg, 79104, Freiburg, Germany
[d] Institute for Organic Chemistry, University of Freiburg, 79104, Freiburg, Germany
[e] Allergy Research Group, Department of Dermatology, Medical Center – University of Freiburg, 79104, Freiburg, Germany
[f] Core Facility Signalling Factory & Robotics, University of Freiburg, 79104, Freiburg, Germany
[g] BIOSS Centre for Biological Signalling Studies, University of Freiburg, 79104, Freiburg, Germany
[h] Max Planck Institute for Medical Research, 69120, Heidelberg, Germany
[i] Institute for Molecular Systems Engineering and Advanced Materials, Heidelberg University, 69120, Heidelberg, Germany
[j] Department of Internal Medicine I, Medical Center - University of Freiburg, 79106, Freiburg, Germany
[k] Institute of Neuropathology, Medical Center - University of Freiburg, 79106, Freiburg, Germany
[l] CIBSS Centre for Integrative Biological Signalling Studies, University of Freiburg, 79104, Freiburg, Germany

ARTICLE INFO

Keywords:
Silicon phthalocyanine
Photoimmunotherapy
Cancer
Pyroptosis
Immunogenic cell death

ABSTRACT

Photoimmunotherapy (PIT) combines the specificity of antibodies with the cytotoxicity of light activatable photosensitizers (PS) and is a promising new cancer therapy. We designed and synthesized, in a highly convergent manner, the silicon phthalocyanine dye WB692-CB2, which is novel for being the first light-activatable PS that can be directly conjugated via a maleimide linker to cysteines. In the present study we conjugated WB692-CB2 to a humanized antibody with engineered cysteines in the heavy chains that specifically targets the prostate-specific membrane antigen (PSMA). The resulting antibody dye conjugate revealed high affinity and specificity towards PSMA-expressing prostate cancer cells and induced cell death after irradiation with red light. Treated cells exhibited morphological characteristics associated with pyroptosis. Mechanistic studies revealed the generation of reactive oxygen species, triggering a cascade of intracellular events involving lipid peroxidation, caspase-1 activation, gasdermin D cleavage and membrane rupture followed by release of pro-inflammatory cellular contents. In first *in vivo* experiments, PIT with our antibody dye conjugate led to a significant reduction of tumor growth and enhanced overall survival in mice bearing subcutaneous prostate tumor xenografts. Our study highlights the future potential of the new phthalocyanine dye WB692-CB2 as PS for the fluorescence-based detection and PIT of cancer, including local prostate tumor lesions, and systemic activation of anti-tumor immune responses by the induction of pyroptosis.

1. Introduction

Photosensitizers (PS) are natural or synthetic compounds that absorb light of a specific wavelength in the ultraviolet, visible or near-infrared light spectrum. After absorption the PS are elevated to an excited state, from which they trigger photosensitization reactions by energy transfer

Peer review under responsibility of KeAi Communications Co., Ltd.
* Corresponding author. Department of Urology, Medical Center – University of Freiburg, 79106, Freiburg, Germany.
** Corresponding author.
E-mail addresses: reinhard.brueckner@organik.chemie.uni-freiburg.de (R. Brückner), philipp.wolf@uniklinik-freiburg.de (P. Wolf).
[1] These authors contributed equally: Isis Wolf, Jonas Storz.

https://doi.org/10.1016/j.bioactmat.2024.07.025
Received 12 September 2023; Received in revised form 30 April 2024; Accepted 17 July 2024
2452-199X/© 2024 The Authors. Publishing services by Elsevier B.V. on behalf of KeAi Communications Co. Ltd. This is an open access article under the CC BY-NC-ND license (http://creativecommons.org/licenses/by-nc-nd/4.0/).

to neighboring molecules, e.g. proteins, nucleic acids or lipids. This can lead to chemical changes resulting in damage and death of target cells or microorganisms [1].

Fluorescent dyes are used as PS in the medical field for the fluorescence-based detection and photodynamic therapy (PDT) of chronic inflammation, drug-resistant bacterial infections or oncological diseases of various types and locations [2]. For the PDT of cancer, the dyes are topically or systemically administered and are selectively irradiated with light to induce cancer cell death. The advantages of PDT over conventional cancer treatments are the use of light without ionizing radiation, the low systemic toxicity of the dyes and the spatiotemporal control of cell death induction in the focus of light [3]. Obstacles for a successful PDT, however, are the hydrophobic characteristics of most dyes that prevent cellular uptake. Therefore, electroporation, liposomes or nanocarriers are applied for enhanced local tissue accumulation. Another problem is the lack of specificity of free PS so that surrounding non-cancerous tissues, that had absorbed the dye, are also damaged after irradiation [4]. PDT can also mean a significant reduction in the quality of life for a patient, as possible skin and eye photosensitivites might require sequestration over several weeks after treatment [5].

To compensate lack of specificity, the dyes can be conjugated to carrier molecules, which specifically bind to antigens of target cells. This technology is called 'targeted PDT' or in particular 'photo-immunotherapy' (PIT), when antibodies or antibody fragments are used [6]. For PIT, fluorescence dyes with absorption peaks in the red or near-infrared (NIR) light (600–1000 nm) are preferred, because they offer deep tissue penetration with reduced scattering and minimal competing absorption by hemoglobin and water [7]. One prominent example is the phthalocyanine dye IRDye®700DX (IR700) [8], which was conjugated to tumor-specific antibodies and antibody fragments for the PIT of various tumor entities [9]. Conjugates consisting of the anti-epidermal growth factor receptor antibody cetuximab and IR700 (ASP-1929) and of an anti-CD25 antibody and IR700 (RM-1995) are currently tested in clinical trials against metastatic or recurrent squamous cell cancer of the head and neck and against advanced or metastatic cutaneous squamous cell cancer (NCT05182866, NCT04305795,

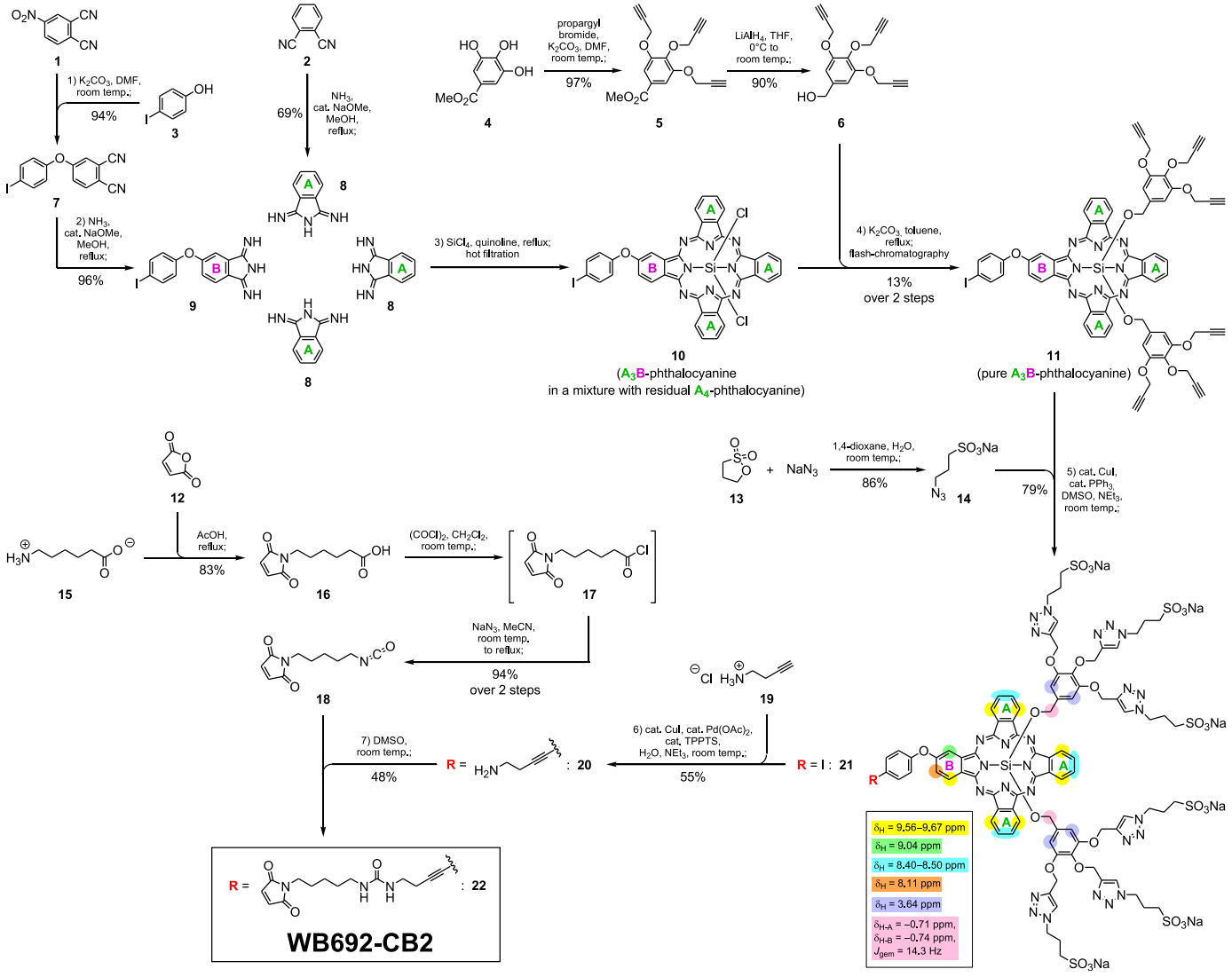

Fig. 1. Synthesis of the A_3B-type silicon phthalocyanine dye WB692-CB2. Preparation of the diiminoisoindolines **8**, which contributes the A parts, and **9**, which contributes the B part, from the phthalodinitriles **2** and **7**, respectively. Cyclocondensation of a 8:1 mixture of these diiminoisoindolines and alcoholysis of the resulting silicon phthalocyanines with the benzyl alcohol **6** delivered the A_3B-type silicon phthalocyanine **11** free from any A_4 analog. All six C≡CH units of compound **11** participated in CuI/PPh_3-catalyzed click reactions with an excess of the sulfonate-containing azide **14**. This rendered the water-soluble silicon phthalocyanine **21** (illustrative ^{1}H NMR chemical shifts at 500.4 MHz in DMSO-d_6). It Sonogashira-coupled with the hydrochloride **19** of but-3-yn-1-ylamine. The silicon phthalocyanine **20**, thereby formed, added to the maleimide-containing isocyanate **18** in the final and just 7th step of our longest linear sequence (cf. step numbering), affording the cysteine-binding silicon phthalocyanine **22** (WB692-CB2).– TPPTS is for trisodium 3,3′,3″-phosphanetriyltris(*meta*-benzenesulfonate).

NCT05265013, NCT03769506, NCT05220748).

In the present study, we synthesized an A_3B-type silicon phthalocyanine dye, called WB692-CB2, which can be bioconjugated and, at the same time, is the first PS, which can be directly coupled to cysteines due to the installment of a maleimide linker. This allows the site-specific coupling of the dye to antibodies with engineered, unpaired cysteine residues for the generation of homogeneous conjugates.

Our synthesis of WB692-CB2 was highly convergent, comprised 7 steps in its longest linear sequence and totaled 14 steps from commercially available starting materials. We conjugated this dye to the humanized antibody h3/F11.19$^{T120C/D265C}$ targeting the prostate specific membrane antigen (PSMA) with modified free cysteines (T120C, D265C) in the heavy chains. The antibody dye conjugate h3/F11.19 $^{T120C/D265C}$-WB692-CB2 was highly effective in the *in vitro* and *in vivo* PIT of PSMA expressing prostate cancer cells. Moreover, we identified pyroptosis as a basic mechanism for PIT-induced cell death.

2. Results

2.1. Synthesis of the A_3B-type silicon phthalocyanine WB692-CB2

We synthesized the first water-soluble A_3B-type phthalocyanine **22**, called WB692-CB2, which is able to bind to cysteine moieties via maleimide-chemistry. As detailed in Fig. 1 and in the *Supplementary Data 1*, our synthesis comprised 14 steps overall yet was effected so convergently that its longest linear sequence consisted of only 7 steps. Kenney established that silicon phthalocyanines without a ring substituent result from the unsubstituted diiminoisoindoline **8**, $SiCl_4$, and an in-situ oxidation [10]. Since then, a variety of ring-substituted silicon phthalocyanines, mostly of the A_4- and rarely of the A_3B-type [11–14], were accessed analogously. We used this strategy for converting an 8:1 mixture of the iminoisoindolines **8** and **9** into the A_3B-type silicon phthalocyanine **10**; **8** (delivering the A-ring) and **9** (delivering the B-ring) were prepared from the underlying phthalonitriles **2** (commercially available) and **7** (obtained from the known ArS_N-reaction between the iodophenol **3** and the phthalonitrile **1** in 94 % rather than 66 % yield [15]) and ammonia in 69 % (ref.: 75 % [16]) and 96 % yield, respectively. The desired A_3B-type dichlorosilicon phthalocyanine **10** contained some of its A_4 analog. The respective mixture and an excess of the benzylic alcohol **6** [prepared from methyl gallate (**4**) by propargylation (97 % yield; ref.: 93 % [17]) and $LiAlH_4$ reduction (90 % yield; ref.: 70 % [17])] underwent a double substitution in the presence of potassium carbonate [18]. It furnished the A_3B-type di (benzyloxy)silicon phthalocyanine **11** pure and in 13 % overall yield from the diiminoisondolines **8** and **9**. All six C≡C bonds of the last-mentioned compound **11** participated in a copper(I)-catalyzed click reaction [19–21] with 3-azidopropansulfonate (**14**) which we obtained from the sultone **13** in 86 % yield (ref.: 85 % [22]); this led to the water-soluble silicon phthalocyanine **21** in 79 % yield. A Sonogashira coupling thereof with but-3-yn-1-ylamine hydrochloride (**19**) in water followed, employing P(*m*-C_6H_4−$SO_3^{\ominus}$ $Na^{\oplus}$)$_3$ ("TPPTS") as a ligand (respective procedure adapted from ref. [23]); this delivered the amino-substituted silicon phthalocyanine **20** in 55 % yield. At this point, the maleimide-containing isocyanate **18** came into the play. We gained it off the longest linear sequence in 3 steps in 78 % yield: 1) a condensation of 6-aminocaproic acid (**15**) with maleic anhydride (**12**) provided the carboxylic acid **16** and our yield (83 %) surpassed the 75 % yield reported by Bui and colleagues [24]; 2) exposure to oxalyl chloride led to the corresponding acid chloride **17**; 3) treatment with sodium azide and rising the temperature to 80 °C induced a Curtius rearrangement and gave the bifunctional isocyanate **18**. We found this modus procedendi better-yielding (94 % yield over the 2 steps) than the 1-step variant using $(PhO)_2P(=O)N_3$; the latter afforded, e. g., a 51 % yield according to Kander et al. [25]. The concluding step of our synthesis was the addition of the amine-containing silicon phthalocyanine **20** to the bifunctional isocyanate **18**. It succeeded by providing 48 % of the cysteine-binding and water-soluble silicon phthalocyanine dye **22** (WB692-CB2).

2.2. Design aspects of the dye WB692-CB2

To the best of our knowledge, the silicon phthalocyanine dye **22** (WB692-CB2) of the present study is only the third compound of bioconjugable silicon phthalocyanine dyes, its sole "predecessors" being the silicon phthalocyanine dyes **23a** (IRDye™ 700DX) [8] and **23b** (PCD 680 NHS [26]; all formulas: Fig. 2). The silicon phthalocyanines **22** and **23a**/**b** differ fundamentally in two regards: Firstly, **22** contains a maleimide moiety for making it bioconjugable with the SH group of protein-based cysteine residues, whereas **23a** and **b** contain a hydroxysuccinimide ester moiety for making them bioconjugable with the NH_2 group of protein-based lysine residues. Secondly, **22** contains Si-bound O−C motifs whereas **23a** and **b** contain Si-bound O−Si motifs. It had been speculated that the somewhat related silicon phthalocyanine **24**, which contains Si-bound O−C motifs, brings about light-induced cell death more efficiently than its analog **25**, which contains Si-bound O−Si motifs [27] (formulas: Fig. 2); such a grading could therefore be shared by our silicon phthalocyanine dye **22** compared to its "predecessors" **23a** and **b**. Moreover, the A_3B-type silicon phthalocyanines **22** and **23a**/**b** differ slightly in another regard, the B-part of **22** being β-substituted vs. the B-part of **23a** and **b** being α-substituted; this causes a welcome bathochromic shift of 12 nm of the absorption maximum of **22** compared to **23a**/**b**.

For the dye WB692-CB2 (**22**) a maximum excitation wavelength of 692 nm and a maximum emission wavelength of 703 nm were determined (Fig. S1a). As a measure of light absorption the extinction coefficient of WB692-CB2 at 692 nm was determined as 116.000 L/(mol x cm) (Fig. S1b). Moreover, the relative fluorescence quantum yield, defined as the ratio of the number of photons emitted to the number of photons absorbed, was calculated to be 0.072 and is thus about half as high as the fluorescence quantum yield of the standard dye IR700, which was published to be 0.14 [8].

WB692-CB2 showed a high photostability. After irradiation with red light at a wavelength of 692 nm and in presence of the electron donor NaAA, a time dependent decrease of absorption was determined up to 48.0 ± 9.0 % after irradiation for 180 min. The photostability of the dye was comparable to that of the control dye IR700 (Fig. S1c).

To verify whether the dye WB692-CB2 is suitable for generating reactive oxygen species for the induction of cell death, the singlet oxygen quantum yield was calculated and determined to be 0.21 ± 0.012 (Fig. S1d). In comparison, the singlet oxygen quantum yield of IR700 was published to be 0.3 [28].

2.3. Generation and characterization of the conjugate h3/F11.19$^{T120C/D265C}$-WB692-CB2

In order to conjugate the dye WB692-CB2 to the humanized anti-PSMA antibody h3/F11.19, free cysteine residues had to be incorporated into the heavy chain of the antibody. The effect of potential cysteine mutations at amino acid sites T120C and D265C (EU numbering), were investigated in a 3D model. There was no evidence that the mutations would interfere with the paratope of the antibody (Fig. 3a). Genes of the heavy chain including the cysteine mutations and the variable domain of the light chain (V_L) were synthesized and cloned into the expression vectors pCSEH1c and pCSL3k for whole IgG heavy and light chain expression, respectively (Fig. 3b). After transfection in Expi293F cells, the expressed antibody h3/F11.19$^{T120C/D265C}$ (Fig. 3c) was detected in high purity in the elution fractions after Protein G affinity chromatography (Fig. S2a). SDS-PAGE analysis under non-reducing and reducing conditions indicated the successful self-assembly of two heavy and two light chains, forming a whole IgG antibody with a predicted size of ~150 kDa (Fig. 3d). The antibody was conjugated with WB692-CB2 (**22**) at a ratio of 1:10, generating the

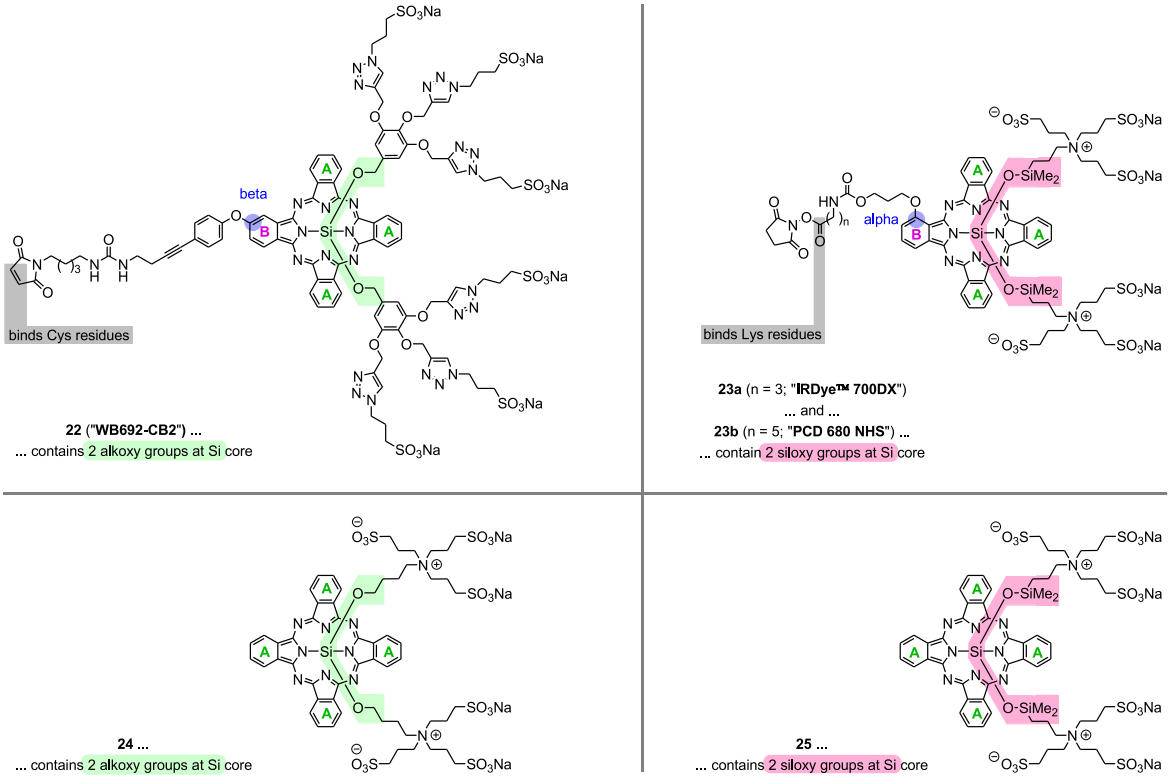

Fig. 2. Design aspects of the A_3B-type silicon phthalocyanine dye WB692-CB2. At top: Juxtaposition of the bioconjugable A_3B-type silicon phthalocyanine structures **22** (WB692-CB2; this work) vs. their only precedents (of sort), namely **23a** (IRDye™ 700DX [8]) and **b** (PCD 680 NHS [26]), both from Peng and Draney et al.; for details, consult the graphics.– At bottom: Juxtaposition of the somewhat related non-bioconjugable A_4-type silicon phthalocyanine structures **24** vs. **25** from a Japanese team [27]; in **24** (judged more promising) and in our silicon phthalocyanine **22**, the silicon atom binds two O−C motifs, while in **25** (judged less promising) and in the earlier silicon phthalocyanines **23a** and **b**, the silicon atom binds two O−Si motifs.

antibody dye conjugate h3/F11.19$^{T120C/D265C}$-WB692-CB2 (Fig. 3e). Protein G affinity chromatography effectively resulted in conjugate preparations without unconjugated dye (Fig. S2b). SDS-PAGE analysis of the conjugate under white and red light (680 ± 10 nm) revealed that the dye was successfully conjugated to the heavy chain of the antibody (Fig. 3f). The dye to antibody ratio was calculated, yielding a mean of 3.4 ± 0.2. For the conjugate h3/F11.19$^{T120C/D265C}$-WB692-CB2, a maximum excitation wavelength of 689 nm and a maximum emission wavelength of 704 nm (Fig. S2c), a fluorescence quantum yield of 0.014 and a singlet oxygen quantum yield of 0.20 ± 0.003 were determined (Fig. S1d).

2.4. PIT of prostate cancer cells with h3/F11.19$^{T120C/D265C}$-WB692-CB2 leads to strong and specific cytotoxicity

The binding properties and cytotoxicity of the conjugate h3/F11.19$^{T120C/D265C}$-WB692-CB2, were tested on prostate cancer cells. We used the prostate cancer cell lines LNCaP and C4-2 with endogenous PSMA expression and the PSMA transduced PC3 cell line PC3-PSMA with exogenous PSMA expression. The PSMA-negative cell line PC3 served as control (Fig. 4a). Flow cytometric analyses revealed binding of the antibody h3/F11.19$^{T120C/D265C}$ to 99.5–100 % of the target cells (Fig. S3a). With the antibody dye conjugate higher K_D values were reached compared to the unconjugated antibody on LNCaP and C4-2 cells with endogenous PSMA expression, whereas the K_D values for both were similar on PC3-PSMA cells with exogenous PSMA expression (Fig. 4b, Figs. S3b–d). This discrepancy can be attributed to differences in PSMA's density on the cell surface, the cellular surface microenvironment surrounding the receptor and the epitope's accessibility [29]. The antibody dye conjugate might be more sensitive to these differences than the unconjugated antibody, particularly if the dye conjugation affects the antibody's flexibility. The differences could be less significant in the PC3-PSMA cells, where PSMA might be more accessible or presented in a less complex microenvironment, leading to similar K_D values for antibody and antibody dye conjugate. No binding was detected with both molecules on PSMA-negative PC3 cells (Fig. 4b, Fig. S3e). This proved that conjugation of the dye did not lead to unspecific binding of the antibody.

For PIT, the prostate cancer cells were incubated with the conjugate followed by irradiation with red light (690 nm) from a LED with an average intensity of 16 mW/cm^2 (Fig. S3f). In a preliminary experiment, dose-dependent cytotoxicity was observed in PC3-PSMA cells (Fig. 4c). Twenty four hours after PIT, cell viability was significantly reduced to 66.7 ± 11.6 % after irradiation with a light dose of 8 J/cm^2 ($p = 0.0382$), whereas only 33.2 ± 5.0 % ($p = 0.0019$) or 4.6 ± 4.6 % ($p = 0.0007$) of the cells survived using light doses of 16 J/cm^2 or 32 J/cm^2, respectively. In the following experiments a light dose of 32 J/cm^2 was used. Control cells were either left untreated or were incubated with equimolar concentrations of antibody or free dye. As shown in Fig. 4d, the viability of conjugate treated LNCaP cells was reduced to 17.2 ± 12.7 % ($p = 0.0020$) 24 h after light exposure. No cytotoxicity was detected in cells treated with antibody or free dye. Moreover, cells of all treatment forms remained unaffected without irradiation. Similar results were obtained in C4-2 and PC3-PSMA cells after treatment with h3/F11.19$^{T120C/D265C}$-WB692-CB2 and a light dose of 32 J/cm^2. Cell viability was significantly reduced to 12.8 ± 8.4 % ($p = 0.0002$; Figs. 4e) and 4.6 ± 4.5 % ($p =< 0.0001$; Fig. 4f), respectively. Nearly all PC3-PSMA cells were killed after light exposure with 32 J/cm^2, which proved that the lower light doses at the edges of the petridishes (3.5 cm in diameter) were also sufficient to perform a successful PIT (Fig. S3f). PC3 cells were completely unaffected by PIT (Fig. 4g). PIT of a mixed PC3-PSMA$^{luc+/GFP+}$/PC3 cell population revealed a specific killing of

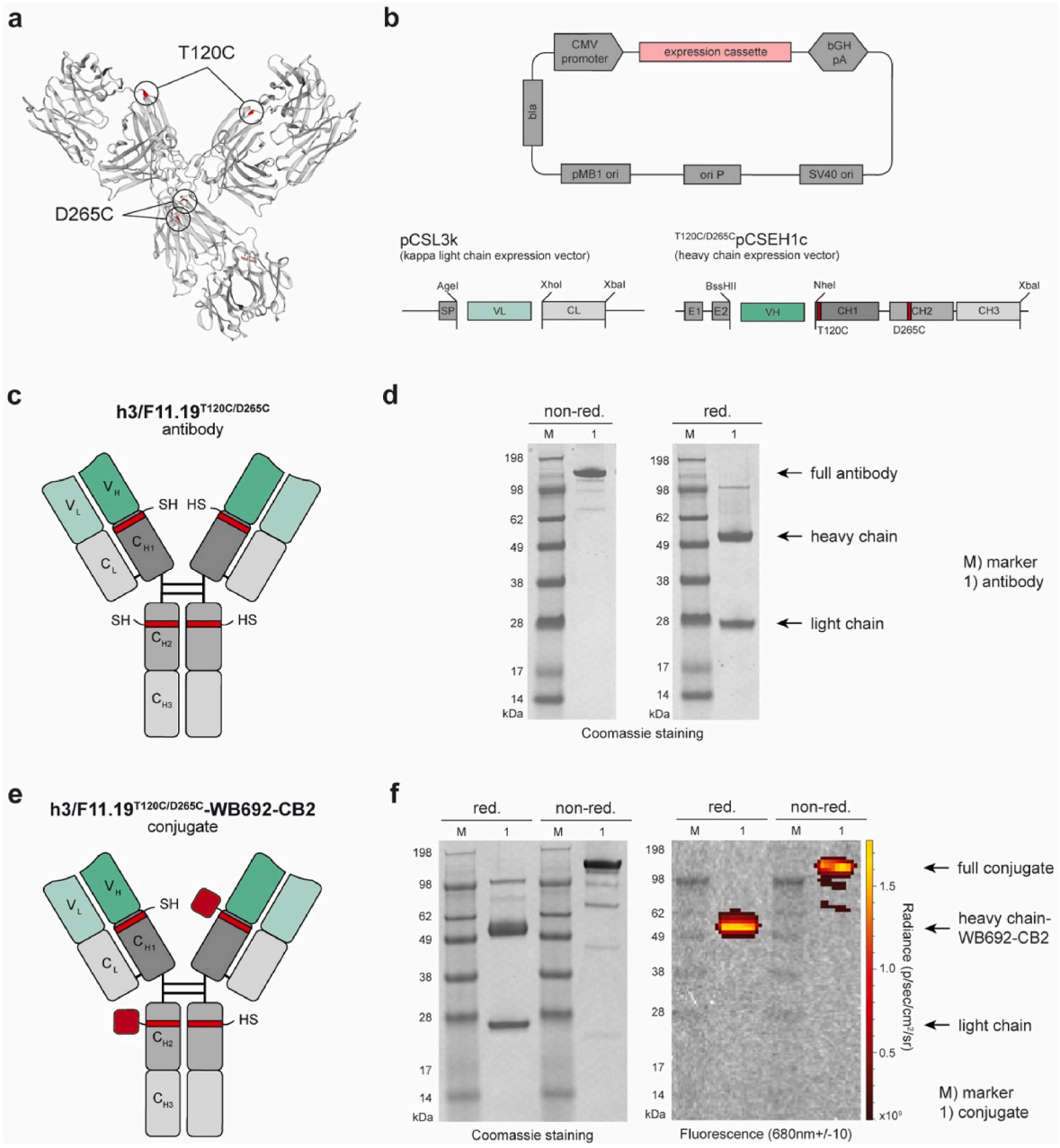

Fig. 3. Generation of the anti-PSMA antibody h3/F11.19$^{T120C/D265C}$ and the antibody dye conjugate h3/F11.19$^{T120C/D265C}$-WB692-CB2. **a** 3D modeling of the anti-PSMA antibody with cysteine mutations in red. **b** Schematic representation of the cloning strategy. **c** Schematic representation of the antibody h3/F11.19$^{T120C/D265C}$. **d** Analysis of the antibody after purification in SDS gels under non-reducing and reducing conditions. **e** Schematic representation of the conjugate h3/F11.19$^{T120C/D265C}$-WB692-CB2. **f** Analysis of the antibody dye conjugate after purification in SDS gels under non-reducing and reducing conditions and under white and red light. Abbreviations: bGH pA, bovine growth hormone poly A signal; bla, ampicillin resistance gene encoding β lactamase; CH1–3 and CL, constant antibody regions of heavy and light chain of IgG1; CMV promoter, cytomegalovirus immediate early promoter; ori P, origin of replication of Epstein-Barr virus (EBV); pMB1 ori, a bacterial origin of replication; SP, secretory mammalian signal peptide; SV40 origin, simian virus (SV) 40 origin of replication; VH and VL, variable antibody regions of light (L) and heavy (H) chain.

the antigen-positive cells (Fig. 4h, Fig. S3g). This underlines that PIT can be a gentle treatment method in which antigen-negative cells in the vicinity of the target cells are spared by the treatment [34]

For different silicon phthalocyanine dyes physical cell membrane stress after axial ligand release was described as a cause of PIT-induced cell death preferably at low oxygen levels [30,31]. We therefore performed the PIT with h3/F11.19$^{T120C/D265C}$-WB692-CB2 on PC3-PSMA cells under hypoxic conditions. As shown in Fig. 4i, PIT in a hypoxic environment of 1 % O_2 was also effective, albeit in a somewhat weaker extend compared to PIT under normoxic conditions (21 % O_2). Twenty-four hours after PIT, cell number was significantly reduced to 21.7 ± 3.2 % ($p < 0.0001$), whereas under normoxic conditions cell number was reduced to 1.8 ± 1 % ($p < 0.0001$).

2.5. *h3/F11.19$^{T120C/D265C}$-WB692-CB2 induces pyroptosis after PIT*

Microscopic analyses revealed blebbing without formation of apoptotic bodies in PSMA-positive prostate cancer cells after PIT (Fig. 5a). Based on these hallmarks, we hypothesized that the cell death mechanism underlying PIT was rather pyroptosis than apoptosis [32].

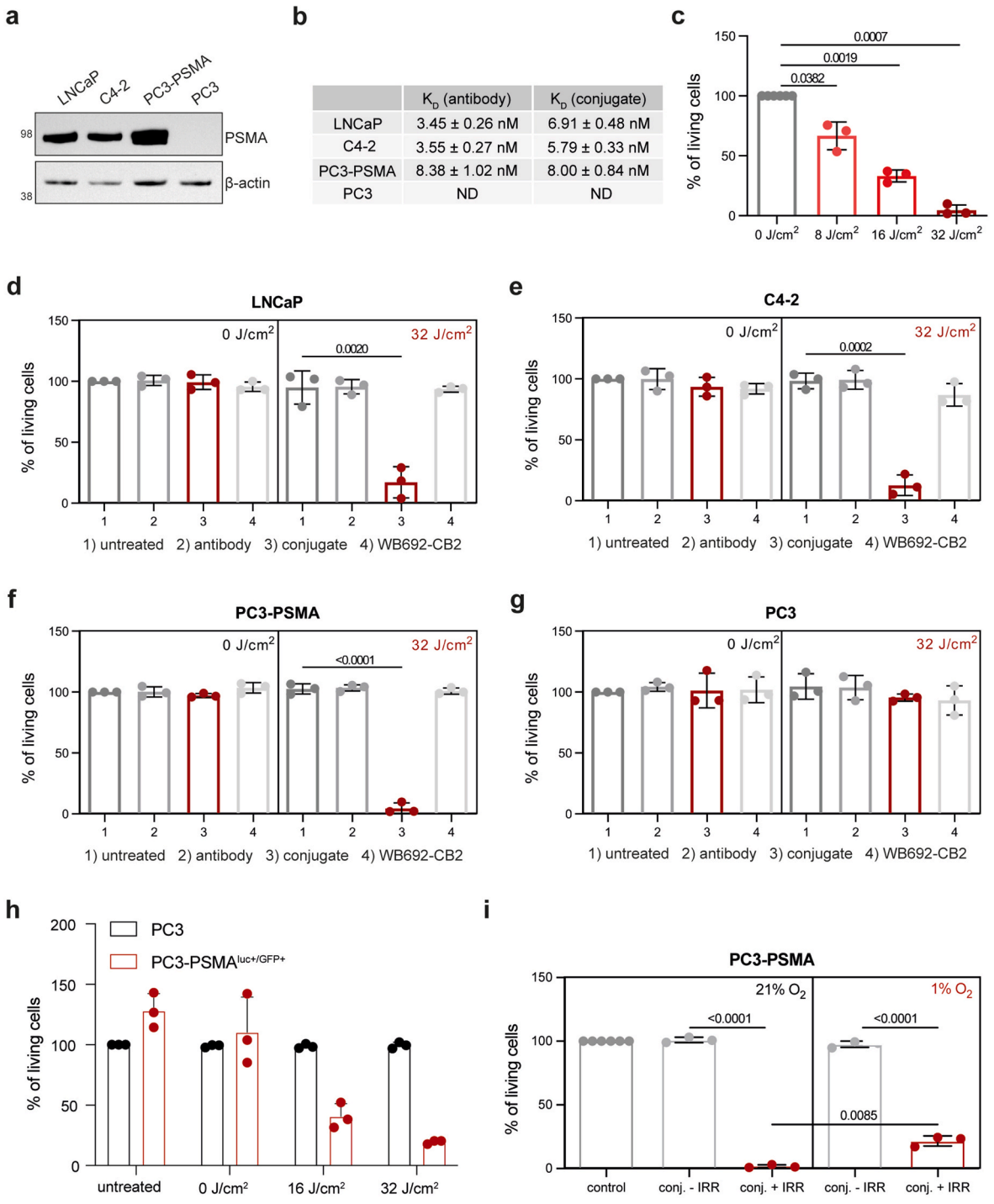

	K_D (antibody)	K_D (conjugate)
LNCaP	3.45 ± 0.26 nM	6.91 ± 0.48 nM
C4-2	3.55 ± 0.27 nM	5.79 ± 0.33 nM
PC3-PSMA	8.38 ± 1.02 nM	8.00 ± 0.84 nM
PC3	ND	ND

Fig. 4. PIT of prostate cancer cells with the antibody dye conjugate h3/F11.19$^{T120C/D265C}$-WB692-CB2. **a** PSMA expression of the prostate cancer cell lines. **b** Cell binding of the antibody h3/F11.19$^{T120C/D265C}$ and the conjugate h3/F11.19$^{T120C/D265C}$-WB692-CB2 as measured by flow cytometry. K_D values were defined as the antibody or conjugate concentrations leading to half-maximal specific binding. **c** Viability of PC3-PSMA cells 24 h after PIT with 10 μg/ml h3/F11.19$^{T120C/D265C}$-WB692-CB2 and increasing light doses. **d** Viability of LNCaP, **e** C4-2, **f** PC3-PSMA and **g** PC3 cells 24 after PIT with 10 μg/ml antibody, 10 μg/ml conjugate, free WB692-CB2 dye or PBS (untreated) and a light dose of 32 J/cm^2. Control cells were not irradiated (0 J/cm^2). **h** Viability of a mixed PC3 and PC3-PSMA$^{luc+/GFP+}$ cell population 24 h after PIT with increasing light doses as determined by flow cytometry. **i** Viability of PC3-PSMA cells 24 h after PIT under normoxic (21 % O_2) or hypoxic (1 % O_2) conditions. Abbreviations: ND, not determinable; conj, conjugate; IRR, irradiation. Mean values ± SD of three independent biological experiments. Statistical analyses by Student's *t*-test (unpaired, parametric with Welch's correction).

We used the cell line PC3-PSMA to further investigate the morphological alterations after PIT. Since pyroptosis is a rapidly emerging cell death, we investigated the cytotoxicity in a time-dependent manner. Directly after irradiation with 32 J/cm^2, cell viability was reduced to 52.6 ± 21.9 % ($p = 0.0646$), whereas e.g. only 27.8 ± 6.6 % ($p = 0.0027$) or 20.5 ± 9.7 % ($p = 0.0049$) of the cells survived 1 h or 3 h after irradiation, respectively (Fig. 5b). Furthermore, the conjugate induced cellular swelling, bleb formation (blue arrows), nuclear condensation without nuclear fragmentation (green arrows) and membrane rupture (pink arrows) shortly after irradiation (Fig. 5c).

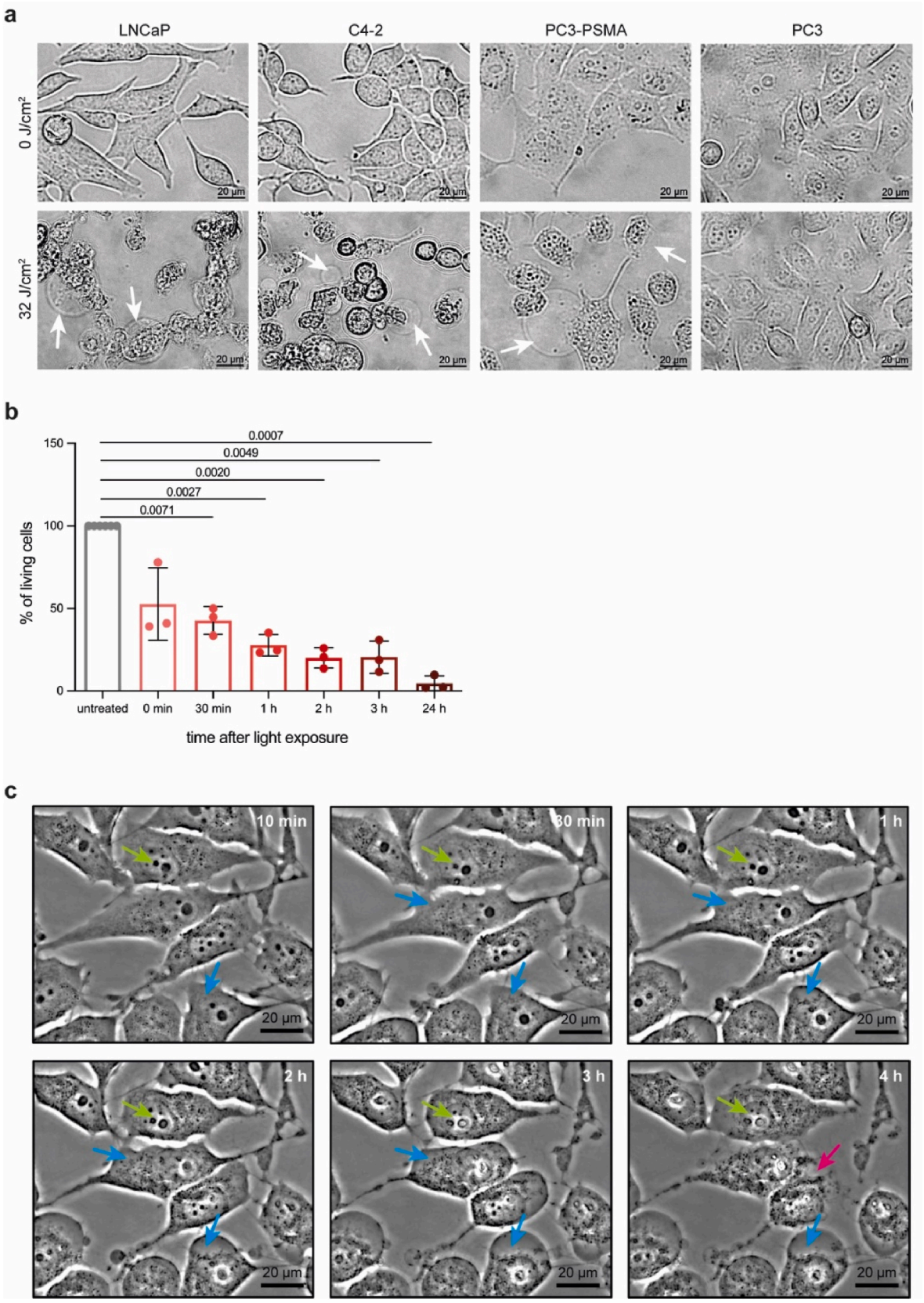

Fig. 5. Morphological changes of prostate cancer cells after PIT. **a** Morphological alterations in prostate cancer cells 24 h after PIT as shown by microscopy. Membrane blebbing is marked by arrows. **b** Time-dependent viability of PC3-PSMA cells after PIT. **b** Time-dependent morphological changes of PC3-PSMA cells after PIT as shown by phase contrast microscopy. Nuclear condensation (green), membrane blebbing (blue) and rupture of the cells (pink) are marked by arrows. Mean values ± SD of three independent biological experiments. Statistical analyses by Student's *t*-test (unpaired, parametric with Welch's correction).

Fluorescence microscopy was performed to visualize the cellular binding of the conjugate h3/F11.19$^{T120C/D265C}$-WB692-CB2. After incubation for 15 min at 37 °C, the fluorescence of the conjugate was detected primarily on the cell surface of PC3-PSMA cells (Fig. 6a, Fig. S4a). Fluorescence was also detected inside the cells after 3–24 h in the perinuclear region, indicating internalization of the conjugate. No binding of the conjugate was observed to PSMA-negative PC3 cells (Fig. S4a). Formation of reactive oxygen species (ROS) has been implicated in the cell death pathways associated with conventional PDT [3]. To examine the formation of ROS during PIT with our dye WB692-CB2, we added the ROS inhibitor N-acetyl-L-cysteine (NAC) to the cells. NAC significantly increased the percentage of living cells 24 h after PIT with a light dose of 16 J/cm^2 from 31.9 ± 5.9 % to 55.9 ± 8.9 % ($p = 0.0058$) (Fig. 6b). To examine a possible lipid peroxidation during PIT, we used the BODIPY 581/591C11 reagent, which fluorescence shifts from ~590 nm (red, FL2) to ~510 nm (green, FL1) during oxidation. In the untreated control cells, most of the BODIPY 581/591C11 signal measured by flow cytometry was in the FL2 channel resulting in a high FL2/FL1 ratio of 284.9 ± 68.6. When the cells were incubated with the h3/F11.19$^{T120C/D265C}$-WB692-CB2 conjugate and irradiated with 16 J/cm^2 or 32 J/cm^2, the FL2/FL1 ratios were significantly lower (45.9 ± 11.2 ($p = 0.0240$) and 29.7 ± 9.3 ($p = 0.0217$), respectively), which indicated that cellular lipid peroxidation is induced during PIT with our conjugate (Fig. 6c).

To further explore the PIT-mediated cell death mechanism, we added the caspase-1 inhibitor Belnacasan (VX-765) to the cells before irradiation with 16 J/cm^2. VX-765 significantly increased the percentage of living cells from 32.3 ± 2.2 % to 47.0 ± 3.5 % ($p = 0.0061$) (Fig. 6d). One of the most prominent hallmarks of pyroptosis is gasdermin D cleavage mediated by activated caspase-1 [33]. We therefore analyzed total gasdermin D and N-terminal gasdermin D levels by Western Blot. Total levels of gasdermin D decreased, while N-terminal gasdermin D levels were increased during PIT over time (Fig. 6e). Furthermore, addition of the gasdermin D inhibitor Disulfiram significantly increased the percentage of living cells from 36.2 ± 2.2 % to 54.4 ± 3.0 % ($p = 0.0015$) (Fig. 6f). Upon cleavage, the N-terminal gasdermin D forms transmembrane pores that release inflammatory cytokines and enable osmotic cell swelling. In this case, Annexin V (AV) as dye for the detection of phosphatidyl serines at the inner side of the cell membrane and Ethidium Homodimer III (EthD-III) as cell impermeable nucleic acid intercalating dye can enter and stain the pyroptotic cells. Indeed, we could find enhanced percentages of AV/EthD-III positive prostate cancer cells after PIT with light doses of 16 and 32 J/cm^2 (Fig. S4b). Finally, pyroptosis leads to rapid rupture of cell membranes and release of cellular contents, such as High-Mobility-Group-Protein B1 (HMGB1), lactate dehydrogenase (LDH) or adenosine triphosphate (ATP). Three hours after PIT, we could detect significantly increased levels of LDH ($p = 0.0416$, Fig. 6g) and ATP ($p = 0.0156$, Fig. 6h) in the supernatant of the cells. Altogether, our results strongly point to pyroptosis as an underlying PIT-induced cell death mechanism with our novel fluorescence dye WB692-CB2.

2.6. *In vivo characterization of h3/F11.19$^{T120C/D265C}$-WB692-CB2*

In first *in vivo* experiments we tested the tumor uptake of the conjugate h3/F11.19$^{T120C/D265C}$-WB692-CB2 in mice bearing subcutaneous PC3-PSMA$^{luc+/GFP+}$ tumor xenografts by bioluminescence imaging (BLI) for the detection of the tumors and by fluorescence imaging (FLI) for the detection of the dye or conjugate. Highest tumor uptake of the conjugate was found 72–96 h after intravenous injection. Moreover, the intratumoral level of the conjugate remained at a high level over several days. In contrast, the free dye WB692-CB2 showed highest tumor uptake 1–5 h after injection followed by a fast tumor clearance (Fig. 7a and Fig. S5a). Biodistribution studies confirmed the high enrichment of the conjugate in the tumors 72 h after injection. A remarkable uptake of the conjugate was detected in the liver. In contrast to the conjugate, the free dye preferentially accumulated in the kidneys (Fig. 7b–S5b).

Next, we tested the *in vivo* PIT with our conjugate h3/F11.19$^{T120C/D265C}$-WB692-CB2 in mice with tumors of about 30–70 mm^3 in size. After two PIT cycles, a significant inhibition of tumor growth was found in animals treated with the conjugate compared to control animals treated with PBS as vehicle (Treatment to Control ratio; TCR: 0.737; one-sided CI: 0.957; Fig. 7c). PIT also resulted in a significant prolonged overall survival of the animals ($p = 0.0105$). Animals, that were treated with PBS or the conjugate and irradiated with red light, had a mean overall survival of 20 or >28 days, respectively (Fig. 7d). No significant weight loss exceeding 20 % as sign of toxicity was measured in any animal during treatment, underlining the high safety of our therapeutic approach (Fig. S5c).

3. Discussion and conclusion

PIT is considered a new cornerstone of local cancer treatment with systemic antitumor effects through induction of immunogenic cell death [34]. We synthesized the new silicon phthalocyanine fluorescence dye WB692-CB2 for the successful application as PS in the PIT of prostate cancer. Our unconjugated dye was found to be non-cytotoxic, which can be attributed to its inherent hydrophilicity, which prevents diffusion through cellular membranes [35]. With h3/F11.19$^{T120C/D265C}$, we used a humanized version of our murine anti-PSMA antibody 3/F11 as binding molecule, which was found to be quickly internalized by multiple receptor-mediated endocytic pathways, including clathrin-mediated endocytosis, macropinocytosis, and clathrin-, caveolae-independent endocytosis [36]. WB692-CB2 was conjugated by a stable covalent linkage to the modified cysteines in the heavy chains of h3/F11.19$^{T120C/D265C}$ using a mild protocol that allowed the dye conjugation to the antibody without interchain disulfide bond disruption. Using this protocol, the dye could also easily be coupled in future to other targeting molecules with free cysteines or thiol groups, e.g. antibody fragments, ligands, peptides or Designed Ankyrin Repeat Proteins (DARPins) for the tailor-made PIT of cancer. Moreover, our conjugation method offers the possibility to specifically influence the pharmacokinetic profile or effector mechanisms of future antibody dye conjugates. For example, aspartic acid at position 265 is involved in the binding of antibodies to Fcγ receptors, a precondition for triggering immunogenic effector mechanisms, such as antibody-dependent cellular cytotoxicity (ADCC) and complement-dependent cytotoxicity (CDC) [37]. Replacement with alanine (D265A), asparagine (D265 N) or glutamic acid (D265E) resulted in reduced affinity to FcγR I, II and III [38]. Since D265 in our conjugate has been replaced by cysteine, the antibody may not be able to perform effector functions. This could minimize infusion reactions of our conjugate in a clinical application. Our conjugate can also be optimized with regard to reduction of serum half-life, e.g. if the time between systemic application of the conjugate and light irradiation in the patient should be shortened. For this, cysteine mutations could be inserted into heavy chain regions responsible for binding to FcRn receptors (e.g. L251-L254, L309-Q311 und N434–H435) [37].

Our conjugate h3/F11.19$^{T120C/D265C}$-WB692-CB2 elicited high and specific cytotoxicity after irradiation with red light in different prostate cancer cells with endogenous or exogenous PSMA expression. Nearly total death of the cancer cells was reached with a light dose of 32 J/cm^2, which can be provided by fiber lasers used in clinical applications [39]. Enhanced efficacy could also be reached by dual targeting, i.e. use of conjugates binding to different tumor-associated antigens [40] or by repeated PIT cycles [41].

Our first *in vivo* studies proved the antitumor activity of our conjugate h3/F11.19$^{T120C/D265C}$-WB692-CB2 in a mouse tumor xenograft model marked by a significant inhibition of tumor growth and a significant enhanced overall survival. The long-lasting tumor retention over several days opens up a large time window for light irradiation after systemic application of the conjugate, which can be advantageous for later clinical application. It differs significantly from an anti-PSMA

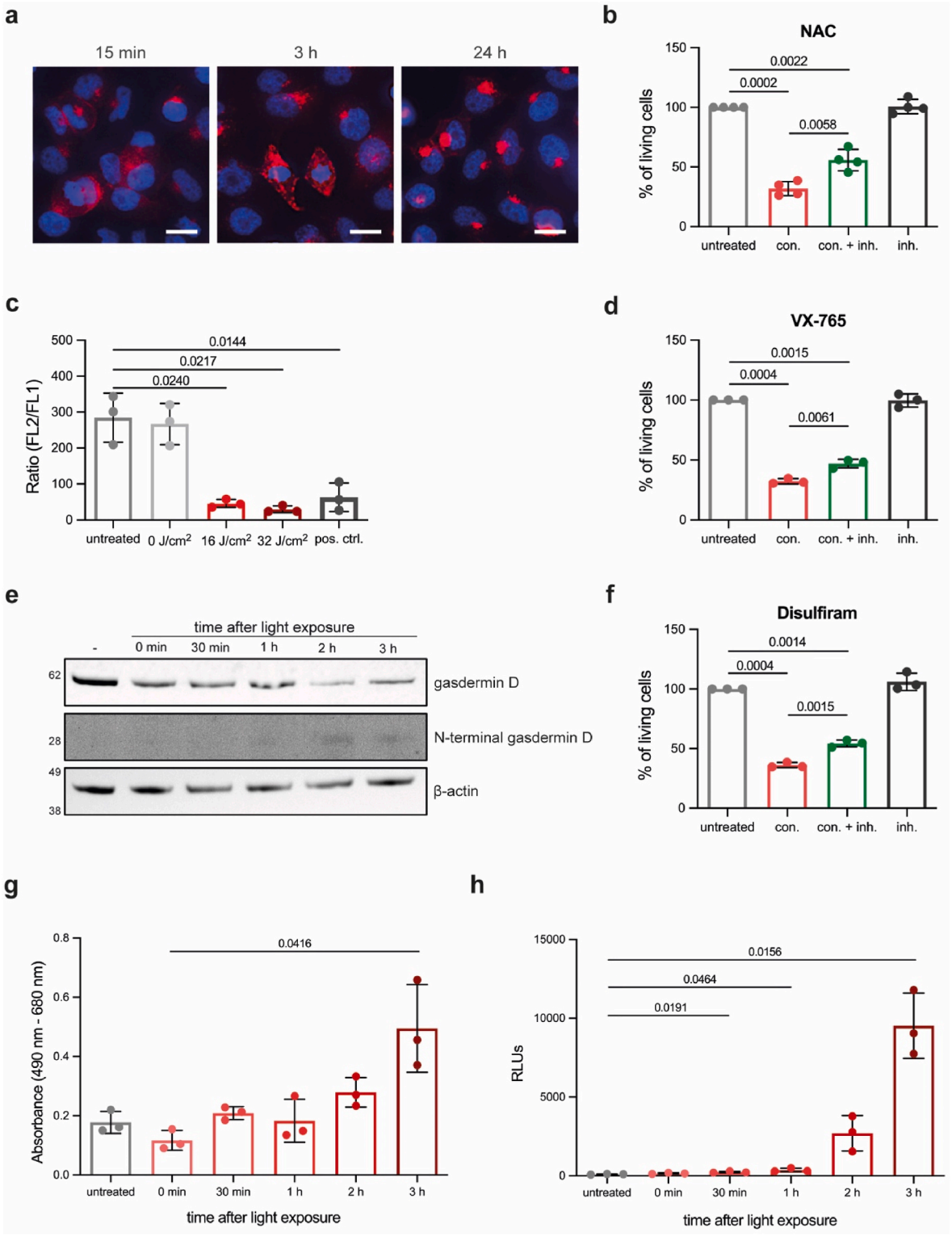

Fig. 6. h3/F11.19$^{T120C/D265C}$-WB692-CB2 induces pyroptosis in PC3-PSMA cells after PIT. **a** Binding and internalization of the conjugate (red) as shown by fluorescence microscopy. Scale bar: 20 μM **b** Viability of cells 24 h after PIT (16 J/cm^2) treated with the ROS inhibitor NAC. **c** Lipid peroxidation of PC3-PSMA cells directly after PIT with irradiation doses of 16 or 32 J/cm^2. Cumene hydroperoxide serve as positive control. **d** Viability of cells 24 h after PIT (16 J/cm^2) treated with the caspase-1 inhibitor VX-765. **e** Western blot analyses of time-dependent gasdermin D cleavage after PIT (16 J/cm^2) **f** Viability of cells 24 h after PIT (16 J/cm^2) treated with the gasdermin D inhibitor Disulfiram. **g** Time-dependent LDH-release after PIT (32 J/cm^2). **h** Time-dependent ATP-release after PIT (32 J/cm^2). Mean values ± SD of three independent biological experiments. Statistical analyses by Student's *t*-test (unpaired, parametric with Welch's correction).

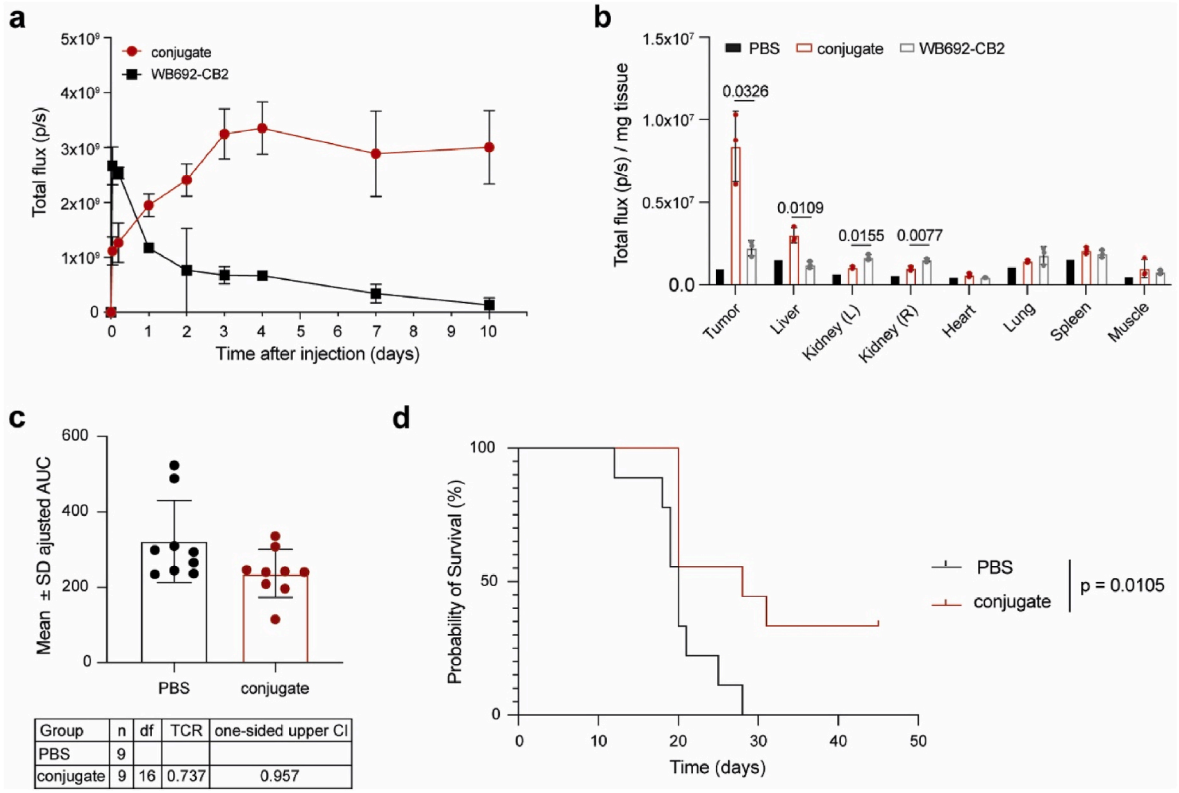

Group	n	df	TCR	one-sided upper CI
PBS	9			
conjugate	9	16	0.737	0.957

Fig. 7. *In vivo* examination of PIT in a subcutaneous PC3-PSMA$^{luc+/GFP+}$ prostate cancer xenograft mouse model. **a** Tumor uptake of conjugate h3/F11.19$^{T120C/D265C}$-WB692-CB2 or free dye WB692-CB2 over a period of 10 days post-injection as shown by fluorescence imaging (FLI). **b** Biodistribution of conjugate or free dye in different organs at the time point of highest tumor uptake (3 days) as shown by FLI. **c** Inhibition of tumor growth after PIT in animals treated with conjugate as determined by time-adjusted area under the curve (AUC). Abbreviations: n, group size; df, degrees of freedom; TCR, Treatment to Control ratio; Cl, one-sided confidence interval for TCR. **d** Survival analysis after PIT of tumor bearing mice treated with PBS (control) or conjugate as determined by Kaplan-Meier analysis and log-rank test with $p < 0.05$.

antibody dye conjugate with the dye IR700, which showed the highest tumor uptake in mice within the first 24 h and which gradually decreased over the following days [42]. Further experiments on the biodistribution and metabolism of the conjugate h3/11. F19$^{T120C/D265C}$-WB692-CB2 are needed to find out what causes the long retention time in the tumors.

We observed that h3/11. F19 $^{T120C/D265C}$-WB692-CB2 induced cell death by irradiation at a time, at which most of the conjugate was already internalized into the prostate cancer cells (24 h after incubation, Fig. 6a). Moreover, cell morphology changes marked by cell swelling, cell blebbing, nuclear condensation and membrane rupture, indicated that the PIT-induced cell death in this study was – at least in part - pyroptosis. Indeed, we could show that light irradiation of our conjugate induced the formation of ROS, lipid peroxidation, caspase-1 activation, cleavage of gasdermin D, membrane rupture and release of ATP and LDH (Fig. 8). We examined the pyroptotic pathway in PC3-PSMA cells with exogenous PSMA expression, which are commonly used as models for investigating therapeutic approaches, including PDT or PIT of PC [42–45]. Since the cell lines LNCaP and C4-2 showed comparable morphological changes after PIT, we assume that these cell lines with endogenous PSMA expression, which are more representative of a clinical situation, undergo the same form of cell death. However, they should also be included in future experiments on PIT-induced cell death.

Pyroptosis was identified as a distinct form of immunogenic cell death (ICD) in 2001 [46]. Generally, it can be induced by bacterial toxins during infections, noncoding RNA or chemicals and is mainly executed by caspase-1 dependent GSDMD cleavage [32]. Formation of GSDMD pores in the plasma membrane causes water influx, cell swelling and eventually cell rupture followed by release of inflammatory Damage Associated Molecular Patterns (DAMPs) and the cytokines IL-1ß and IL-18 [47]. Pyroptosis in cancer cells produces neoantigens, which are processed by antigen-presenting cells for the formation of antigen-specific cytotoxic T cells. It thus provides a great opportunity for the induction of a systemic immune response for long term control of cancer and for synergism with immune checkpoint blockade [48,49]. In recent years, induction of pyroptosis by PDT, chemotherapy or radiotherapy came into focus as a novel anti-cancer therapy, however in an unspecific manner with damage of immune cells or hematopoietic cells and related side effects [50]. With our WB692-CB2 based PIT this problem can be solved, because targeted pyroptosis in tumor cells can be induced. Our approach is promising for tumor lesions that can be reached with light and may already have developed resistance to apoptosis. For the treatment of prostate cancer, WB692-CB2 based PIT can be performed as focal therapy with preservation of the prostate gland or during robotic-assisted radical prostatectomy for the detection and treatment of residual tumor cells in areas, where surgery cannot be continued. This could lead to complete tumor elimination and thus avoidance of local recurrence.

Our observation that WB692-CB2-based PIT induces pyroptosis, does not exclude that other cell death mechanisms described for other silicon phthalocyanine dyes [30,31] may also be triggered after irradiation of the dye. As a main mechanism release of axial ligands from the core domain upon light irradiation, followed by alteration in hydrophilicity and aggregation of the dye, is discussed. When the dye is coupled to an antigen bound antibody, this leads to physical changes in the shape of the antigen-antibody complex, induction of physical stress of the cellular membrane, cellular influx of water and finally necrotic cell death [30,31]. Such reactions can preferably occur under low oxygen conditions and in presence of an electron donor, like cellular glutathione, and allow the uncaging of small molecules, e.g. inhibitors, to attack cancer cells

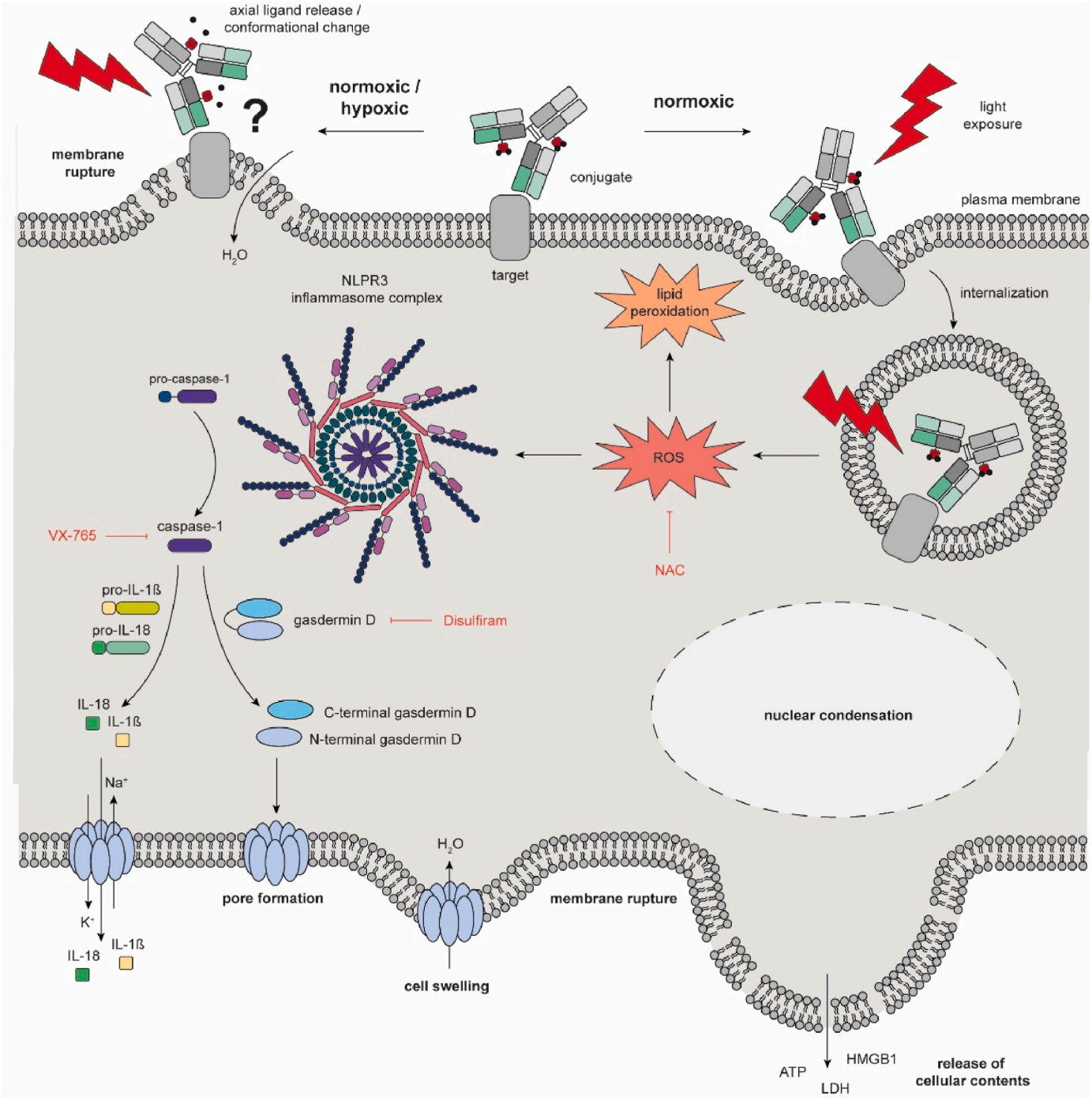

Fig. 8. Molecular mechanisms of PIT-mediated pyroptosis.
The conjugate h3/F11.19$^{T120C/D265C}$-WB692-CB2 binds to its target (PSMA) on the surface of prostate cancer cells and is internalized by multiple receptor-mediated endocytic pathways. After irradiation and normoxic conditions, the photosensitizer absorbs photons and generates reactive oxygen species (ROS) by a photochemical reaction, leading to lipid peroxidation and activation of caspase-1. Activated caspase-1 cleaves the proinflammatory cytokines pro-IL-1β/18 and the autoinhibited gasdermin D (GSDMD). Upon processing, the N-terminal GSDMD forms a transmembrane pore in the plasma membrane, which is permeable for ions, small molecules (e.g. IL-1β and IL-18) and water. Pore formation destroys osmotic balance, allowing water influx leading to cell swelling, membrane blebbing and finally rupture of the cells. Nuclear condensation during pyroptosis is also observed, but nuclear integrity is maintained. After membrane rupture, cellular contents (such as lactate dehydrogenase (LDH), high mobility group box 1 (HMGB1) or adenosine triphosphate (ATP)) are released, serving as pro-inflammatory signals. The inhibitors NAC, VX-765, and Disulfiram are able to inhibit PIT-mediated cell death partially. Alternatively, a cell death mechanism, that has been described for other silicon phthalocyanines (e.g. IR700) could also be triggered. Irradiation of the antigen-bound conjugate could lead to cleavage of the axial ligands from WB692-CB2, resulting in decreased solubility and aggregation of the antigen-antibody complex. This physical stress on the cell membrane could increase transmembrane water flow, eventually leading to cell bursting and necrotic cell death [30].

under hypoxic conditions [31]. Since we have shown that the absorption of our dye decreased after irradiation as a possible sign for cleavage of its axial ligands and that PIT with our dye worked in a weakened form also under hypoxic conditions, this main mechanism can also be assumed in addition to pyroptosis. Future experiments that analyze the aggregation behavior and examine the photochemical and physical reactions of WB692-CB2 at the molecular level can shed light on this in future. Effective PIT under hypoxic conditions is particularly desirable for prostate tumors, as these are characterized by a low oxygen content [51].

In summary, it is conceivable that after internalization of our conjugate and under normoxic conditions, pyroptosis is preferentially triggered, while after antigen binding and under normoxic or hypoxic conditions the axial ligands of WB692-CB2 are released and the cell membranes are physically damaged (Fig. 8). Both cases mean rapid induction of cellular stress and cell death leading to an activation of the immune system, so that local PIT can be used to achieve a systemic effect against cancer cells that have already spread or metastasized.

4. Materials and methods

4.1. Synthesis of the silicon phthalocyanine dye WB692-CB2

All synthetic procedures were conducted with standard laboratory equipment. Synthetic intermediates were either too sensitive for being purified (**8**, **9** and **10**) or resulted so pure that they needed no purification (**6**, **7**, **14**, **16** and **18**), were purified by crystallization (**5**), by flash chromatography on normal silica gel (**11**) [52] or by flash chromatography on reversed-phase silica gel (**20**, **21** and **22**). A detailed description of the dye synthesis can be found in the *Supplementary Data 1*.

4.2. 3D modeling of the antibody h3/F11.19$^{T120C/D265C}$

A 3D model was generated using the SWISS-MODEL protein structure homology-modeling server (Protein Structure Bioinformatics Group, Swiss Institute of Bioinformatic, Biozentrum, University of Basel, Switzerland) [53–57].

4.3. Generation of h3/F11.19$^{T120C/D265C}$

Genes of the heavy chain including the mutations T120C and D265C (EU numbering) and the variable domain of the light chain (V_L) of the humanized anti-PSMA antibody h3/F11.19 were synthesized (GeneArt, Invitrogen, Regensburg, Germany) and cloned into the expression vectors pCSEH1c and pCSL3k containing constant domains of a human IgG1 antibody for whole heavy and light chain expression, respectively. After transformation of the vectors into XL1-BlueMRF' supercompetent *E. coli* cells (Agilent Technologies, Waldbronn, Germany) and purification with the NucleoBond® Xtra Maxi Kit (Cat. No. 7440414.10, Macherey-Nagel, Düren, Germany), correct sequences of the heavy and light chain of h3/F11.19$^{T120C/D265C}$ were verified by sequencing (Microsynth Seqlab, Göttingen, Germany). Recombinant antibody expression in EXPI293F cells was performed as described before [58]. The antibody was purified by protein G affinity chromatography (Cytiva, Marlborough, USA), dialyzed against PBS and the protein concentration was determined by Pierce BCA Protein Assay Kit (Thermo Fischer Scientific).

4.4. Generation of the antibody dye conjugate h3/F11.19$^{T120C/D265C}$-WB692-CB2

The antibody h3/F11.19$^{T120C/D265C}$ in PBS containing 1 mM EDTA (pH 7.4) was reduced with 40 equimolar Tris-(2-Carboxyethyl)phosphine, Hydrochloride (TCEP, Carl Roth, Karlsruhe, Germany) for 3 h at 37 °C. After dialysis against PBS, 1 mM EDTA (pH 7.4) at 4 °C overnight, the antibody was re-oxidized with 30 equimolar dehydroascorbic acid (Sigma-Aldrich, St. Louis, USA) for 4 h at room temperature. For conjugation, the antibodies were incubated with 10 x equimolar WB692-CB2 at room temperature for 1 h. To quench the reaction, 25 equimolar N-acetyl-L-cysteine (Sigma-Aldrich) was added for 15 min, followed by overnight dialysis against PBS (pH 7.4). Unbound dye was removed by protein G affinity chromatography (Cytiva) and dialysis against PBS. Successful conjugation and purification of the conjugate h3/F11.19$^{T120C/D265C}$-WB692-CB2 was verified by SDS-PAGE under reducing or non-reducing conditions using Coomassie staining (Protein Ark, Sheffield, UK) and fluorescence-based imaging (λ_{max} = 680 nm, IVIS Spectrum, In Vivo Imaging System, PerkinElmer, Waltham, USA). The protein concentration was determined by using the Pierce BCA Protein Assay Kit (Thermo Fischer Scientific, Waltham, USA). The degree of labeling was calculated according to the TechTip#31 protocol "Calculate dye:protein (F/P) molar ratios" (Thermo Fischer Scientific).

4.5. Excitation and emission spectra

The dye WB692-CB2 and the conjugate h3/F11.19$^{T120C/D265C}$-WB692-CB2 were diluted to a concentration of 62.5 µg/ml in water and transferred into NuncTM 384 well transparent Flat Bottom plates. Water was used as control. Excitation spectra were measured using a microplate reader (Biotek Synergy H4, GEN5 Version 2.01.13, Agilent Technologies, Santa Clara, CA, USA) in the wavelength range from 300 to 750 nm in 5 nm steps. For the emission spectra, the samples were transferred into a Nunc™ 384 well Black Flat Bottom plate and the excitation was fixed to one wavelength while the fluorescence wavelength was screened from 500 to 900 nm in 5 nm steps.

4.6. Extinction coefficient

For the determination of the extinction coefficient, the dye was dissolved in H_20 and excitation was measured at different concentrations using a UV-1900i spectrophotometer (Shimadzu Deutschland GmbH, Duisburg, Germany).

4.7. Relative fluorescence quantum yield

The dye WB692-CB2 and the conjugate h3/F11.19$^{T120C/D265C}$-WB692-CB2 were measured at concentrations of 0, 0.5, 0.75, 1, 1.5 and 2 µM for absorption at 692 nm in a Varian Cary® 50 UV–Vis spectrophotometer (Agilent Tech., Santa Clara, CA, USA). Integrated fluorescence spectra at 650–850 nm were determined using a 1 cm Quartz cuvette in a Cary Eclipse Fluorescence Spectrometer (Agilent Tech.). IR700 (LICOR Bioscience, Lincoln, NE, USA) was used as reference. The gradient value of each compound was obtained from the linear fit of A_{692nm} and integrated fluorescence.

Equation for relative Fluorescence Quantum Yield (ϕ):

$$\phi_X = \phi_{ST}\left[\frac{m_X}{m_{ST}}\right]\left[\frac{\eta_X^2}{\eta_{ST}^2}\right]$$

with ϕ = fluorescence quantum yield;

ST and X = standard and test, respectively;
m = gradient from the plot of integrated fluorescence intensity vs absorbance;
η = refractive index of the solvent.

4.8. Photostability

For the photostability experiment, 5 µM WB692-CB2 or IR700 in PBS (pH 7.5) with or without 1 mM L-ascorbic acid sodium salt (NaAA) as electron donor were irradiated (16 mW/cm^2) with a red light-emitting diode (LED, λ_{max} = 690 nm, L690-66-60, Marubeni, Tokyo) for up to 3 h. Before and at different time points during irradiation, 100 µl samples were collected in a 96-well plate and absorbances were determined

using the IVIS Imaging System with an appropriate filter set and the Living Image Software.

4.8.1. Singlet oxygen quantum yield

For the determination of the singlet oxygen quantum yield, 500 nM of the dye WB692-CB2 or the conjugate h3/F11.19$^{T120C/D265C}$-WB692-CB2 were mixed in 50 mM phosphate buffer (pH 7.5), 10 mM Imidazole and 50 μM N,*N*-Dimethyl-4-Nitrosoanilin (RNO, Sigma Aldrich) as scavenger. Measurement was done at room temperature (25 °C) in 96-well transparent plates with 200 μl mixture for each well. The samples were irradiated with red light from the LED ($\lambda_{ma}\lambda_x = 690$ nm, 30 mW/cm^2) and absorption was measured every 30 s over 10 min. Quenching of RNO was measured at OD 440 nm. Absorptions of the dye or conjugate were measured before irradiation at 692 nm. IR700 with a singlet oxygen quantum yield of 0.3 [28], was used as reference. Buffer without dyes was used as blank. The experiment was performed in three replicates.

Singlet oxygen quantum yields of WB692-CB2 and h3/F11.19$^{T120C/D265C}$-WB692-CB2 (samples) were calculated according to the equation:

$$\phi_{\Delta sam} = \phi_{\Delta ref} \times [(m_{sam}/m_{ref}) \times (L_{ref}/L_{sam})]$$

With $\phi\Delta_{sam}$ = singlet oxygen quantum yield of the samples.

$\phi\Delta_{ref}$ = singlet oxygen quantum yield of the reference dye IR700,
m_{sam} = slope in changes of RNO absorbance at OD 440 nm against photoirradiation time using dye WB692-CB2,
m_{ref} = slope in changes of RNO absorbance at OD 440 nm against photoirradiation time using reference dye IR700,
L_{sam} = light harvesting efficiency of target dye WB692-CB2, at photoirradiation wavelength ($L = 1–10^{-A}$, with "*A*" = absorbance at the photoirradiation (photoexcitation) wavelength).
L_{ref} = light harvesting efficiencies of the reference dye IR700, at photoirradiation wavelength ($L = 1–10^{-A}$, with "A" = absorbance at the photoirradiation (photoexcitation) wavelength).

4.9. Cells and inhibitors

The PSMA-positive prostate cancer cell lines LNCaP and C4-2 and the PSMA-negative cell line PC3 were obtained from ATCC (Manassas, VA, USA). The PSMA transduced cell line PC3-PSMA was kindly provided by P. Giangrande (University of Iowa) and transduced with luciferase/GFP as described [59]. All cells were cultivated in RPMI1640 medium (Gibco, Invitrogen, Karlsruhe, Germany) supplemented with 10 % fetal calf serum (Sigma Aldrich, St. Louis, USA) and penicillin/streptomycin (100 U/mL, 100 mg/L) at 37 °C and 5 % CO_2. Cell line identities were verified using short tandem repeat (STR) analysis (CLS GmbH, Eppelheim, Germany). The ROS inhibitor N-acetyl-L-cysteine (NAC) was purchased from Sigma-Aldrich and dissolved as 0.1 M stock solution in PBS. The caspase-1 inhibitor Belnacasan (VX-765) was dissolved as 100 mg/ml stock solution in DMSO and stored at −80 °C. The gasdermin D (GSDMD) inhibitor Disulfiram was purchased from Selleck Chemicals LLC (Houston, USA), dissolved as 40 mM stock solution in DMSO and stored at −80 °C.

4.10. Flow cytometric analyses

Specific binding of the produced antibodies or conjugates to the prostate cancer cells was tested by flow cytometry as described [60] using a goatanti-human Ig (H + L)-RPE detection antibody (Southern Biotech, Birmingham, USA). Mean fluorescence values of stained cells were determined with a FACS Calibur Flow Cytometer and the CellQuest software (BD Biosciences, Heidelberg, Germany). Binding affinity of the antibodies was calculated with help of the GraphPad Prism 7 software (GraphPad Software Inc., San Diego, USA) and dissociation constants (K_D) were defined as the antibody or conjugate concentrations leading to half-maximal specific binding. Quantification of apoptotic and necrotic cells after treatment was analyzed using the Apoptosis and Necrosis Quantification Kit Plus, according to manufacturer's protocol (Biotium, Fremont, USA). Lipid peroxidation directly after PIT was measured by using the Image-iT™ Lipid Peroxidation Kit (Thermo Fisher Scientific) according to the manufacturer's instructions.

4.11. Microscopy and fluorescence microscopy

Cell morphology after PIT was examined by microscopy with or without phase contrast using a Zeiss AxioObserver Z.1 inverted microscope (Carl Zeiss Microscopy GmbH, Munich, Germany). To analyze the internalization of the conjugate, cells were incubated with 20 μg/ml h3/F11.19$^{T120C/D265C}$-WB692-CB2 for different time spans and mounted with Vectashield® Antifade Mounting Medium with DAPI (Biozol, Eching, Germany). The samples were analyzed using the Olympus scanR widefield microscopy system (Olympus, Shinjuku, Japan).

4.12. PIT of prostate cancer cells

For PIT, 2.5 x 10^5 cancer cells were seeded in 35 mm cell culture dishes (Thermo Fischer Scientific) and cultivated for 24 h in the incubator (37 °C, 5 % CO_2). On the next day, the cell culture medium was removed and cells were treated with medium as control, 10 μg/ml antibody, 10 μg/ml conjugate or the equimolar amount of free dye for 24 h. For the inhibition of caspase-1 activation and GSDMD cleavage, 100 μM VX-765 or 1 μM Disulfiram were added. For the inhibition of ROS 5 mM NAC were added 1 h before light exposure. Then cells were washed with PBS, incubated in fresh medium and irradiated with red light at various intensities and exposure times. The intensity incident on the cells was determined as follows: a photodetector (S142C, Thorlabs, Newton, USA) with a 1 mm opening was scanned in the plane of the cells to record the intensity profile with an optical power meter (PM100, Thorlabs, Newton, USA). The data were fitted to a Gauß amplitude function and the mean intensity was determined to be 16 mW/cm^2. After PIT (0 min–24 h), the cells were trypsinized, stained with the vital dye Erythrosine b (Logos Biosystems, Gyeonggi-do, South Korea) followed by cell viability analysis with a Neubauer Counting Chamber. Cell numbers of living cells were normalized relative to the untreated control establishing a baseline of 100 %.

For mixed *in vitro* PIT, 1.25x10^5 luciferase/GFP-transduced PC3-PSMA$^{luc+/GFP}$ cells and 1.25x10^5 PC3 cells were mixed and seeded in 35 mm cell culture dishes. PIT was performed as described above. Twenty-four hours after PIT, the cells were trypsinized and cell numbers were counted using a flow cytometer. The acquisition was stopped automatically, when the sample reached 5000 events in the stopping gate (PC3 cell population). Cell numbers of living cells were normalized relative to the untreated controls establishing a baseline of 100 %.

For in vitro PIT under hypoxic conditions, PC3-PSMA cells were prepared as described above. One hour before PIT, the cells were transferred to the Whitley i2 Instrument Workstation (Meintrup DWS Laborgeräte GmbH, Herzlake, Germany) set to 1 % O_2 and the culture medium was replaced with fresh medium that has been pre-equilibrated overnight at 1 % O_2. After acclimatization in the Workstation, the cells were irradiated with red light from the LED ($\lambda_{max} = 690$ nm, 32 J/cm^2). Twenty-four hours later, cell viability was analyzed as described above.

4.13. SDS-PAGE and Western blot analyses

Antibodies and conjugates were analyzed after purification via SDS-PAGE under reducing and non-reducing conditions according to the manufacturer's instructions (Invitrogen, Carlsbad, CA, USA). For Western blot analysis, cell pellets were lysed in 50 mM Tris-HCl, 150 mM NaCl, 1 mM EDTA, 0.5 % NaDeoxycholate, 0.05 % SDS, 1 % Igepal after PIT. Protein content was determined by using the Quick Bradford Protein Assay (Bio-Rad Laboratories, Inc., Hercules, USA). 50–100 μg

protein per lane were blotted onto nitrocellulose membranes. PSMA expression on target cells was verified by using the anti-PSMA antibody K7 [61] and horse radish peroxidase (HRP)-labeled polyclonal rabbit anti-mouse IgG (Dako, Hamburg, Germany). Gasdermin cleavage was detected using the rabbit antiN-terminal GSDMD antibody (Abcam, Cambridge, USA) and (HRP)-labeled goat anti-rabbit IgG (Dako, Hamburg, Germany). Monoclonal mouse anti-actin HRP-conjugated antibody was used as loading control (Proteintech Group, Inc., Rosemont, USA). Western blots were developed with an enhanced chemiluminescence (ECL) system and protein bands were detected and analyzed using an INTAS Chemo Star Imager and the Software ChemoStar (INTAS Science Imaging Instruments, Göttingen, Germany).

4.14. ATP and LDH release

Cellular release of adenosine 5′-triphosphate (ATP) or lactate dehydrogenase (LDH) after PIT was analyzed by CellTiter-Glo 2.0 Cell Viability Assay (Promega, Madison, USA) or CyQUANT LDH Cytotoxicity Assay Kit (Invtitrogen, Waltham, USA), respectively, according to the manufacturers' protocols. Luminescence (as relative luminescence units, RLUs) or absorbance were measured with a Synergy HTX ELISA-reader (BioTek, Winooski, USA).

4.14.1. Animal studies

Animal studies were performed in accordance with the German animal protection law and with permission from the responsible local authorities (RP Freiburg, G-23/029). Male Athymic Nude mice (Rj: ATHYM-Foxn1$^{nu/nu}$ mice, 6–8 weeks old, Janvier Labs, Saint-Berthevin, France) were kept under sterile and standardized environmental conditions.

For measurement of the tumor uptake, animals (n = 2–3 per group) were subcutaneously injected with 1x10^6 luciferase-transduced PC3-PSMA$^{luc+/GFP+}$ cells in 100 µl PBS mixed with 100 µl Matrigel® (Corning, Kaiserslautern, Germany) into the right flank. Tumors were detected through palpation, and their sizes were measured using an electronic caliper. The volumes of the tumors were determined using the formula V = (d^{2}xD)/2, where "d" represents the smaller and "D" the larger diameter of the tumor. When the tumors reached a volume of approximately 30–70 mm^3 (= day 0), the animals were injected intravenously with 100 µg h3/F11.19$^{T120C/D265C}$-WB692-CB2 or an equimolar amount of WB692-CB2 in 100 µl PBS. Tumor uptake was detected by *in vivo* bioluminescence imaging (BLI) in combination with fluorescence imaging (FLI) 0, 1, and 5 h, as well as 1, 2, 3, 4, 7, and 10 days after conjugate or dye administration. For this, 150 mg/kg luciferin (BioSynth AG, Staad, Switzerland) was injected intraperitoneally into the mice, followed by imaging under anesthesia using the IVIS Vision Imaging System. Regions of interests (ROIs) were placed over the tumors and tumor uptake of the conjugate or dye was measured by determining the total fluxes (p/s) of the tumors.

For biostribution studies, tumor bearing animals (n = 1–3 per group) were treated with the conjugate, dye or PBS (control) and euthanised at the time point of highest tumor uptake, which was determined in the previous tumor uptake study. Excised organs were weighed and analyzed for conjugate or dye uptake by FLI imaging.

For *in vivo* PIT, Nude mice (n = 9 per group) were subcutaneously injected with 1x10^6 PC3-PSMA$^{luc+/GFP+}$ cells in 100 µl PBS mixed with 100 µl Matrigel®. Animals bearing tumors with a volume of 30–70 mm^3 were intravenously injected with 100 µg h3/F11.19$^{T120C/D265C}$-WB692-CB2 or 100 µl PBS, respectively (= day 0 of treatment), followed by a second injection on day 10. Red light irradiation of the tumors with doses of 100 J/cm^2 was performed on days 3, 5, 11 and 13 under anesthesia using the LED (λ = 690 ± 10 nm, 50 mW/cm^2). Measurement of the tumor volumes was performed as described above until day 45 of treatment. Animals were euthanized earlier, if any of the following terminal criteria were met: largest tumor diameter >15 mm, ulcerating tumor or weight loss >20 % over two consecutive days.

4.15. Statistical analyses

All statistical analyses were performed using the GraphPad Prism software (GraphPad Software Inc., San Diego, USA). Data were presented as mean ± standard deviation (SD) from at least three independent experiments unless otherwise indicated. Significance of the data was calculated with the Student's *t*-test (unpaired, parametric with Welch's correction).

For *in vivo* experiments, inhibition of tumor growth was quantified by calculating the time adjusted Area Under the Curve (AUC) using R (https://www.R-project.org/) following the method described by Wu and Houghton [62]. Values between the data points were interpolated by applying the linear trapezoidal method. Significance of the time-adjusted AUC data was used to estimate the inhibition effect by determining the ratio of the means for treatment and control (TCR). An inhibition effect was considered significant, when the upper limit of Fieller's one-sided 95 % confidence interval remained below 1 [63].

Ethics approval and consent to participate

The ethics review committee of the regional supervisory authority Regierungspräsidium Freiburg, Freiburg, Germany, approved the animal experiment protocol (G-23/029).

CRediT authorship contribution statement

Isis Wolf: Data curation, Formal analysis, Investigation, Methodology, Validation, Writing – original draft. **Jonas Storz:** Data curation, Formal analysis, Investigation, Methodology, Validation, Writing – original draft. **Susanne Schultze-Seemann:** Data curation, Formal analysis, Methodology, Validation. **Philipp R. Esser:** Conceptualization, Data curation, Formal analysis, Methodology, Validation, Writing – original draft. **Stefan F. Martin:** Resources, Supervision, Writing – review & editing. **Susan Lauw:** Formal analysis, Methodology, Validation, Writing – original draft. **Peer Fischer:** Formal analysis, Methodology, Writing – original draft. **Marie Peschers:** Formal analysis. **Wolfgang Melchinger:** Formal analysis, Methodology, Validation, Writing – review & editing. **Robert Zeiser:** Methodology, Resources, Writing – review & editing. **Oliver Gorka:** Methodology, Resources, Writing – review & editing. **Olaf Groß:** Resources, Writing – review & editing. **Christian Gratzke:** Resources, Writing – review & editing. **Reinhard Brückner:** Conceptualization, Funding acquisition, Project administration, Resources, Supervision, Writing – original draft, Writing – review & editing. **Philipp Wolf:** Conceptualization, Funding acquisition, Project administration, Resources, Supervision, Writing – original draft, Writing – review & editing.

Declaration of competing interest

None.

Acknowledgements

We thank P. Giangrande (University of Iowa) for the PC3-PSMA cells, E.V. Wenzel and S. Dübel (University of Braunschweig) for providing the cloning vectors and M. Follow (Lighthouse Core Facility, University Medical Center, University of Freiburg) for support with fluorescence microscopy. This work was funded by the German Research Foundation (DFG, grant no. WO 2178/3–1 to PW), the Federal Ministry of Economic Affairs and Climate Action (BMWK, grant no. 03THW15H04 to RB and PW) and supported by the Open Access Publication Fund of the University of Freiburg. We thank Dr. E. Mymrikov, Institute of Biochemistry and Molecular Biology, University of Freiburg, for providing his support, laboratory and instruments for dye characterization.

Appendix A. Supplementary data

Supplementary data to this article can be found online at https://doi.org/10.1016/j.bioactmat.2024.07.025.

References

[1] M.S. Baptista, J. Cadet, A. Greer, A.H. Thomas, Photosensitization reactions of biomolecules: definition, targets and mechanisms, Photochem. Photobiol. 97 (2021) 1456–1483, https://doi.org/10.1111/php.13470.

[2] S. Kwiatkowski, B. Knap, D. Przystupski, J. Saczko, E. Kędzierska, K. Knap-Czop, J. Kotlińska, O. Michel, K. Kotowski, J. Kulbacka, Photodynamic therapy - mechanisms, photosensitizers and combinations, Biomed. Pharmacother. 106 (2018) 1098–1107, https://doi.org/10.1016/j.biopha.2018.07.049.

[3] P. Agostinis, K. Berg, K.A. Cengel, T.H. Foster, A.W. Girotti, S.O. Gollnick, S. M. Hahn, M.R. Hamblin, A. Juzeniene, D. Kessel, M. Korbelik, J. Moan, P. Mroz, D. Nowis, J. Piette, B.C. Wilson, J. Golab, Photodynamic therapy of cancer: an update, CA A Cancer J. Clin. 61 (2011) 250–281, https://doi.org/10.3322/caac.20114.

[4] J.C.S. Simões, S. Sarpaki, P. Papadimitroulas, B. Therrien, G. Loudos, Conjugated photosensitizers for imaging and PDT in cancer Research, J. Med. Chem. 63 (2020) 14119–14150, https://doi.org/10.1021/acs.jmedchem.0c00047.

[5] J.H. Correia, J.A. Rodrigues, S. Pimenta, T. Dong, Z. Yang, Photodynamic therapy review: principles, photosensitizers, applications, and future directions, Pharmaceutics 13 (2021) 1332.

[6] D. Mew, C.K. Wat, G.H. Towers, J.G. Levy, Photoimmunotherapy: treatment of animal tumors with tumor-specific monoclonal antibody-hematoporphyrin conjugates, J. Immunol. 130 (1983) 1473–1477, https://doi.org/10.4049/jimmunol.130.3.1473.

[7] J.V. Frangioni, In vivo near-infrared fluorescence imaging, Curr. Opin. Chem. Biol. 7 (2003) 626–634, https://doi.org/10.1016/j.cbpa.2003.08.007.

[8] X. Peng, D. Draney, W. Volcheck, G. Bashford, D. Lamb, D. Grone, Y. Zhang, C. Johnson, Phthalocyanine dye as an extremely photostable and highly fluorescent near-infrared labeling reagent, SPIE BiOS 6097 (2006). SPIE.

[9] Y. Maruoka, H. Wakiyama, P.L. Choyke, H. Kobayashi, Near infrared photoimmunotherapy for cancers: a translational perspective, EBioMedicine 70 (2021) 103501, https://doi.org/10.1016/j.ebiom.2021.103501.

[10] M.K. Lowery, A.J. Starshak, J.N. Esposito, P.C. Krueger, M.E. Kenney, Dichloro (phthalocyanino)silicon, Inorg. Chem. 4 (1965) 128, https://doi.org/10.1021/ic50023a036, 128.

[11] V. Nemykin, E. Lukyanets, Synthesis of substituted phthalocyanines, ARKIVOC (Gainesville, FL, U. S.) 2010 (2010), https://doi.org/10.3998/ark.5550190.0011.104.

[12] X. Li, B.-D. Zheng, X.-H. Peng, S.-Z. Li, J.-W. Ying, Y. Zhao, J.-D. Huang, J. Yoon, Phthalocyanines as medicinal photosensitizers: developments in the last five years, Coord. Chem. Rev. 379 (2019) 147–160, https://doi.org/10.1016/j.ccr.2017.08.003.

[13] K. Mitra, M.C.T. Hartman, Silicon phthalocyanines: synthesis and resurgent applications, Org. Biomol. Chem. 19 (2021) 1168–1190, https://doi.org/10.1039/D0OB02299C.

[14] P. Saha, S. Das, H.K. Indurthi, D.K. Sharma, Advancement in use of silicon pthalocyanine derivatives for cancer treatment, Dyes Pigments 206 (2022) 110608, https://doi.org/10.1016/j.dyepig.2022.110608.

[15] C.B. Kc, G.N. Lim, M.E. Zandler, F. D'Souza, Synthesis and photoinduced electron transfer studies of a tri(phenothiazine)-subphthalocyanine-fullerene pentad, Org. Lett. 15 (2013) 4612–4615, https://doi.org/10.1021/ol402274k.

[16] P.-C. Lo, S. Wang, A. Zeug, M. Meyer, B. Röder, D.K.P. Ng, Preparation and photophysical properties of halogenated silicon(IV) phthalocyanines substituted axially with poly(ethylene glycol) chains, Tetrahedron Lett. 44 (2003) 1967–1970, https://doi.org/10.1016/S0040-4039(03)00061-3.

[17] J. Camponovo, J. Ruiz, E. Cloutet, D. Astruc, New polyalkynyl dendrons and dendrimers: "click" chemistry with azidomethylferrocene and specific anion and cation electrochemical sensing properties of the 1,2,3-triazole-containing dendrimers, Chemistry 15 (2009) 2990–3002, https://doi.org/10.1002/chem.200801999.

[18] J.N. Esposito, J.E. Lloyd, M.E. Kenney, The synthesis and physical properties of some organo- and organosiloxysilicon phthalocyanines, Inorg. Chem. 5 (1966) 1979–1984, https://doi.org/10.1021/ic50045a031.

[19] C.W. Tornøe, M. Meldal, Peptidotriazoles: copper(I)-Catalyzed 1,3-dipolar cycloadditions on solid-phase, in: M. Lebl, R.A. Houghten (Eds.), Peptides: the Wave of the Future: Proceedings of the Second International and the Seventeenth American Peptide Symposium, June 9–14, 2001, San Diego, California, U.S.A., Springer Netherlands, Dordrecht, 2001, pp. 263–264.

[20] C.W. Tornøe, C. Christensen, M. Meldal, Peptidotriazoles on solid phase: [1,2,3]-triazoles by regiospecific copper(i)-catalyzed 1,3-dipolar cycloadditions of terminal alkynes to azides, J. Org. Chem. 67 (2002) 3057–3064, https://doi.org/10.1021/jo011148j.

[21] V.V. Rostovtsev, L.G. Green, V.V. Fokin, K.B. Sharpless, A stepwise huisgen cycloaddition process: copper(I)-catalyzed regioselective "ligation" of azides and terminal alkynes, Angew Chem. Int. Ed. Engl. 41 (2002) 2596–2599, https://doi.org/10.1002/1521-3773(20020715)41:14<2596::aid-anie2596>3.0.co;2-4.

[22] S.K. Samanta, D. Moncelet, B. Vinciguerra, V. Briken, L. Isaacs, Metal organic polyhedra: a click-and-clack approach toward targeted delivery, Helv. Chim. Acta 101 (2018), https://doi.org/10.1002/hlca.201800057.

[23] D.T. Bong, M.R. Ghadiri, Chemoselective Pd(0)-catalyzed peptide coupling in water, Org. Lett. 3 (2001) 2509–2511, https://doi.org/10.1021/ol016169e.

[24] Q.A. Bui, T.H.H. Vu, V.K.T. Ngo, I.R. Kennedy, N.A. Lee, R. Allan, Development of an ELISA to detect clenbuterol in swine products using a new approach for hapten design, Anal. Bioanal. Chem. 408 (2016) 6045–6052, https://doi.org/10.1007/s00216-016-9750-2.

[25] T. Kantner, A.G. Watts, Characterization of reactions between water-soluble trialkylphosphines and thiol alkylating reagents: implications for protein-conjugation reactions, Bioconjugate Chem. 27 (2016) 2400–2406, https://doi.org/10.1021/acs.bioconjchem.6b00375.

[26] X. Peng, D.R. Draney, J. Chen, Phthalocyanine Dyes. US-Patent 7,005, 518 B2, 2006. February 26th.

[27] H. Takakura, S. Matsuhiro, M. Kobayashi, Y. Goto, M. Harada, T. Taketsugu, M. Ogawa, Axial-ligand-cleavable silicon phthalocyanines triggered by near-infrared light toward design of photosensitizers for photoimmunotherapy, J. Photochem. Photobiol. Chem. 426 (2022) 113749, https://doi.org/10.1016/j.jphotochem.2021.113749.

[28] S. Kishimoto, M. Bernardo, K. Saito, S. Koyasu, J.B. Mitchell, P.L. Choyke, M. C. Krishna, Evaluation of oxygen dependence on in vitro and in vivo cytotoxicity of photoimmunotherapy using IR-700-antibody conjugates, Free Radic. Biol. Med. 85 (2015) 24–32, https://doi.org/10.1016/j.freeradbiomed.2015.03.038.

[29] M. Hadzhieva, A.D. Pashov, S. Kaveri, S. Lacroix-Desmazes, H. Mouquet, J. D. Dimitrov, Impact of antigen density on the binding mechanism of IgG antibodies, Sci. Rep. 7 (2017) 3767, https://doi.org/10.1038/s41598-017-03942-z.

[30] K. Sato, K. Ando, S. Okuyama, S. Moriguchi, T. Ogura, S. Totoki, H. Hanaoka, T. Nagaya, R. Kokawa, H. Takakura, M. Nishimura, Y. Hasegawa, P.L. Choyke, M. Ogawa, H. Kobayashi, Photoinduced ligand release from a silicon phthalocyanine dye conjugated with monoclonal antibodies: a mechanism of cancer cell cytotoxicity after near-infrared photoimmunotherapy, ACS Cent. Sci. 4 (2018) 1559–1569, https://doi.org/10.1021/acscentsci.8b00565.

[31] E.D. Anderson, A.P. Gorka, M.J. Schnermann, Near-infrared uncaging or photosensitizing dictated by oxygen tension, Nat. Commun. 7 (2016) 13378, https://doi.org/10.1038/ncomms13378.

[32] X. Wei, F. Xie, X. Zhou, Y. Wu, H. Yan, T. Liu, J. Huang, F. Wang, F. Zhou, L. Zhang, Role of pyroptosis in inflammation and cancer, Cell. Mol. Immunol. 19 (2022) 971–992, https://doi.org/10.1038/s41423-022-00905-x.

[33] J. Shi, Y. Zhao, K. Wang, X. Shi, Y. Wang, H. Huang, Y. Zhuang, T. Cai, F. Wang, F. Shao, Cleavage of GSDMD by inflammatory caspases determines pyroptotic cell death, Nature 526 (2015) 660–665, https://doi.org/10.1038/nature15514.

[34] M.A. Hsu, S.M. Okamura, C.D. De Magalhaes Filho, D.M. Bergeron, A. Rodriguez, M. West, D. Yadav, R. Heim, J.J. Fong, M. Garcia-Guzman, Cancer-targeted photoimmunotherapy induces antitumor immunity and can be augmented by anti-PD-1 therapy for durable anticancer responses in an immunologically active murine tumor model, Cancer Immunol. Immunother. 72 (2023) 151–168, https://doi.org/10.1007/s00262-022-03239-9.

[35] R. Zhang, X. Qin, F. Kong, P. Chen, G. Pan, Improving cellular uptake of therapeutic entities through interaction with components of cell membrane, Drug Deliv. 26 (2019) 328–342, https://doi.org/10.1080/10717544.2019.1582730.

[36] J. Liu, P. Kopeckova, P. Buhler, P. Wolf, H. Pan, H. Bauer, U. Elsasser-Beile, J. Kopecek, Biorecognition and subcellular trafficking of HPMA copolymer-anti-PSMA antibody conjugates by prostate cancer cells, Mol. Pharm. 6 (2009) 959–970, https://doi.org/10.1021/mp8002682.

[37] X. Wang, M. Mathieu, R.J. Brezski, IgG Fc engineering to modulate antibody effector functions, Protein Cell 9 (2018) 63–73, https://doi.org/10.1007/s13238-017-0473-8.

[38] R.L. Shields, A.K. Namenuk, K. Hong, Y.G. Meng, J. Rae, J. Briggs, D. Xie, J. Lai, A. Stadlen, B. Li, J.A. Fox, L.G. Presta, High resolution mapping of the binding site on human IgG1 for Fc gamma RI, Fc gamma RII, Fc gamma RIII, and FcRn and design of IgG1 variants with improved binding to the Fc gamma R, J. Biol. Chem. 276 (2001) 6591–6604, https://doi.org/10.1074/jbc.M009483200.

[39] G. Shafirstein, D. Bellnier, E. Oakley, S. Hamilton, M. Potasek, K. Beeson, E. Parilov, Interstitial photodynamic therapy-A focused review, Cancers 9 (2017), https://doi.org/10.3390/cancers9020012.

[40] H. Sato, K. Noma, T. Ohara, K. Kawasaki, M. Akai, T. Kobayashi, N. Nishiwaki, T. Narusaka, S. Komoto, H. Kashima, Y. Katsura, T. Kato, S. Kikuchi, H. Tazawa, S. Kagawa, Y. Shirakawa, H. Kobayashi, T. Fujiwara, Dual-targeted near-infrared photoimmunotherapy for esophageal cancer and cancer-associated fibroblasts in the tumor microenvironment, Sci. Rep. 12 (2022) 20152, https://doi.org/10.1038/s41598-022-24313-3.

[41] M. Mitsunaga, T. Nakajima, K. Sano, P.L. Choyke, H. Kobayashi, Near-infrared theranostic photoimmunotherapy (PIT): repeated exposure of light enhances the effect of immunoconjugate, Bioconjugate Chem. 23 (2012) 604–609, https://doi.org/10.1021/bc200648m.

[42] T. Nagaya, Y. Nakamura, S. Okuyama, F. Ogata, Y. Maruoka, P.L. Choyke, H. Kobayashi, Near-infrared photoimmunotherapy targeting prostate cancer with prostate-specific membrane antigen (PSMA) antibody, Mol. Cancer Res. 15 (2017) 1153–1162, https://doi.org/10.1158/1541-7786.mcr-17-0164.

[43] X. Wang, R. Sun, J. Wang, J. Li, E. Walker, A. Shirke, G. Ramamurthy, L. Shan, D. Luo, L. Carmon, J.P. Basilion, A low molecular weight multifunctional theranostic molecule for the treatment of prostate cancer, Theranostics 12 (2022) 2335–2350, https://doi.org/10.7150/thno.68715.

[44] E. Walker, S.M. Turaga, X. Wang, R. Gopalakrishnan, S. Shukla, J.P. Basilion, J. D. Lathia, Development of near-infrared imaging agents for detection of junction adhesion molecule-A protein, Transl Oncol 14 (2021) 101007, https://doi.org/10.1016/j.tranon.2020.101007.

[45] M. Capozza, R. Stefania, V. Dinatale, V. Bitonto, L. Conti, C. Grange, R. Skovronova, E. Terreno, A novel PSMA-targeted probe for NIRF-guided surgery and photodynamic therapy: synthesis and preclinical validation, Int. J. Mol. Sci. 23 (2022), https://doi.org/10.3390/ijms232112878.
[46] B.T. Cookson, M.A. Brennan, Pro-inflammatory programmed cell death, Trends Microbiol. 9 (2001) 113–114, https://doi.org/10.1016/s0966-842x(00)01936-3.
[47] S.L. Fink, B.T. Cookson, Caspase-1-dependent pore formation during pyroptosis leads to osmotic lysis of infected host macrophages, Cell Microbiol. 8 (2006) 1812–1825, https://doi.org/10.1111/j.1462-5822.2006.00751.x.
[48] Y. Fang, Y. Tang, B. Huang, Pyroptosis: a road to next-generation cancer immunotherapy, Semin. Immunol. 68 (2023) 101782, https://doi.org/10.1016/j.smim.2023.101782.
[49] Q. Wang, Y. Wang, J. Ding, C. Wang, X. Zhou, W. Gao, H. Huang, F. Shao, Z. Liu, A bioorthogonal system reveals antitumour immune function of pyroptosis, Nature 579 (2020) 421–426, https://doi.org/10.1038/s41586-020-2079-1.
[50] Y. Tan, Q. Chen, X. Li, Z. Zeng, W. Xiong, G. Li, X. Li, J. Yang, B. Xiang, M. Yi, Pyroptosis: a new paradigm of cell death for fighting against cancer, J. Exp. Clin. Cancer Res. 40 (2021) 153, https://doi.org/10.1186/s13046-021-01959-x.
[51] O.A.A. Mohamed, H.S. Tesen, M. Hany, A. Sherif, M.M. Abdelwahab, M. H. Elnaggar, The role of hypoxia on prostate cancer progression and metastasis, Mol. Biol. Rep. 50 (2023) 3873–3884, https://doi.org/10.1007/s11033-023-08251-5.
[52] W.C. Still, M. Kahn, A. Mitra, Rapid chromatographic technique for preparative separations with moderate resolution, J. Org. Chem. 43 (1978) 2923–2925, https://doi.org/10.1021/jo00408a041.
[53] A. Waterhouse, M. Bertoni, S. Bienert, G. Studer, G. Tauriello, R. Gumienny, F. T. Heer, T.A.P. de Beer, C. Rempfer, L. Bordoli, R. Lepore, T. Schwede, SWISS-MODEL: homology modelling of protein structures and complexes, Nucleic Acids Res. 46 (2018) W296–w303, https://doi.org/10.1093/nar/gky427.
[54] N. Guex, M.C. Peitsch, T. Schwede, Automated comparative protein structure modeling with SWISS-MODEL and Swiss-PdbViewer: a historical perspective, Electrophoresis 30 (Suppl 1) (2009) S162–S173, https://doi.org/10.1002/elps.200900140.
[55] S. Bienert, A. Waterhouse, T.A. de Beer, G. Tauriello, G. Studer, L. Bordoli, T. Schwede, The SWISS-MODEL Repository-new features and functionality, Nucleic Acids Res. 45 (2017) D313–d319, https://doi.org/10.1093/nar/gkw1132.
[56] G. Studer, C. Rempfer, A.M. Waterhouse, R. Gumienny, J. Haas, T. Schwede, QMEANDisCo-distance constraints applied on model quality estimation, Bioinformatics 36 (2020) 1765–1771, https://doi.org/10.1093/bioinformatics/btz828.
[57] M. Bertoni, F. Kiefer, M. Biasini, L. Bordoli, T. Schwede, Modeling protein quaternary structure of homo- and hetero-oligomers beyond binary interactions by homology, Sci. Rep. 7 (2017) 10480, https://doi.org/10.1038/s41598-017-09654-8.
[58] F. Bertoglio, D. Meier, N. Langreder, S. Steinke, U. Rand, L. Simonelli, P.A. Heine, R. Ballmann, K.T. Schneider, K.D.R. Roth, M. Ruschig, P. Riese, K. Eschke, Y. Kim, D. Schäckermann, M. Pedotti, P. Kuhn, S. Zock-Emmenthal, J. Wöhrle, N. Kilb, T. Herz, M. Becker, M. Grasshoff, E.V. Wenzel, G. Russo, A. Kröger, L. Brunotte, S. Ludwig, V. Fühner, S.D. Krämer, S. Dübel, L. Varani, G. Roth, L. Čičin-Šain, M. Schubert, M. Hust, SARS-CoV-2 neutralizing human recombinant antibodies selected from pre-pandemic healthy donors binding at RBD-ACE2 interface, Nat. Commun. 12 (2021) 1577, https://doi.org/10.1038/s41467-021-21609-2.
[59] J. Mastroianni, N. Stickel, H. Andrlova, K. Hanke, W. Melchinger, S. Duquesne, D. Schmidt, M. Falk, G. Andrieux, D. Pfeifer, H. Dierbach, A. Schmitt-Graeff, F. Meiss, M. Boerries, R. Zeiser, miR-146a controls immune response in the melanoma microenvironment, Cancer Res. 79 (2019) 183–195, https://doi.org/10.1158/0008-5472.can-18-1397.
[60] M. Michalska, S. Schultze-Seemann, L. Bogatyreva, D. Hauschke, U. Wetterauer, P. Wolf, In vitro and in vivo effects of a recombinant anti-PSMA immunotoxin in combination with docetaxel against prostate cancer, Oncotarget 7 (2016) 22531–22542, https://doi.org/10.18632/oncotarget.8001.
[61] U. Elsässer-Beile, P. Wolf, D. Gierschner, P. Bühler, W. Schultze-Seemann, U. Wetterauer, A new generation of monoclonal and recombinant antibodies against cell-adherent prostate specific membrane antigen for diagnostic and therapeutic targeting of prostate cancer, Prostate 66 (2006) 1359–1370, https://doi.org/10.1002/pros.20367.
[62] J. Wu, P.J. Houghton, Interval approach to assessing antitumor activity for tumor xenograft studies, Pharmaceut. Stat. 9 (2010) 46–54, https://doi.org/10.1002/pst.369.
[63] L.A. Hothorn, Statistical analysis of in vivo anticancer experiments: tumor growth inhibition, Drug Inf. J. 40 (2006) 229–238, https://doi.org/10.1177/009286150604000212.